A novel isoform of MAP4 organises the paraxial microtubule array required for muscle cell differentiation

Binyam Mogessie[1,2], Daniel Roth[1], Zainab Rahil[1,3] and Anne Straube[1,*]

[1] Centre for Mechanochemical Cell Biology, Warwick Medical School, University of Warwick, Coventry, CV4 7AL, UK

[2] Current address: MRC Laboratory of Molecular Biology, Cell Biology Division, Cambridge, CB2 0QH, UK

[3] Current address: Department of Chemical and Biomolecular Engineering, University of Illinois, Urbana-Champaign, IL 61801, USA

* Correspondence should be addressed to A.S (e-mail: anne@mechanochemistry.org)

ABSTRACT

The microtubule cytoskeleton is critical for muscle cell differentiation and undergoes reorganisation into an array of paraxial microtubules, which serves as template for contractile sarcomere formation. Here, we identify a previously uncharacterised isoform of microtubule-associated protein MAP4, oMAP4, as a microtubule organising factor that is crucial for myogenesis. We show that oMAP4 is expressed upon muscle cell differentiation and is the only MAP4 isoform essential for normal progression of the myogenic differentiation programme. Depletion of oMAP4 impairs cell elongation and cell-cell fusion. Most notably, oMAP4 is required for paraxial microtubule organisation in muscle cells and prevents dynein- and kinesin-driven microtubule-microtubule sliding. Purified oMAP4 aligns dynamic microtubules into antiparallel bundles that withstand motor forces *in vitro*. We propose a model in which the cooperation of dynein-mediated microtubule transport and oMAP4-mediated zippering of microtubules drives formation of a paraxial microtubule array that provides critical support for the polarisation and elongation of myotubes.

INTRODUCTION

Skeletal muscle fibre formation requires a coordinated programme of morphological and biochemical changes in the differentiating cells. Upon differentiation, mono-nucleated myoblasts withdraw from the cell cycle and fuse to form syncytial myotubes (Wakelam, 1985). The microtubule cytoskeleton is required for these processes (Bischoff and Holtzer, 1968, Holtzer et al., 1975, Toyama et al., 1982) and undergoes reorganisation into an array of paraxial microtubules (Warren, 1974), which serves as template for contractile sarcomere formation (Antin et al., 1981, Pizon et al., 2005).

During myogenesis, microtubules are rearranged from a dynamic, radial array to a parallel array of stable, posttranslationally modified microtubules within the elongating cell (Warren, 1974, Saitoh et al., 1988, Tassin et al., 1985, Gundersen et al., 1989). Preventing detyrosination of tubulin or interfering with microtubule stabilisation by depletion of EB1 or MURF, impairs expression of myogenic markers (Zhang et al., 2009, Spencer et al., 2000, Chang et al., 2002), thus suggesting that signalling through modified microtubules might control myogenic differentiation. On the other hand, changes in the regulation of microtubule dynamics at the cell cortex that neither affect the content of tubulin modifications nor the expression of differentiation markers, can result in cell polarisation and fusion defects as caused by the depletion of EB3 (Straube and Merdes, 2007). This suggests a dual function of microtubules during the early stages of muscle cell differentiation to control (1) morphological changes and (2) biochemical composition, before later serving as structural templates for myofibrillogenesis.

A number of microtubule-associated proteins (MAPs) have been implicated in the organisation of microtubules into bundles. MAP2 and tau determine the spacing between microtubules in dendrites and axons, but do not control the directionality of microtubules within those bundles (Chen et al., 1992). Proteins of the PRC1/MAP65/Ase1 family preferentially bundle microtubules in antiparallel orientation and are responsible for the stabilisation of the antiparallel microtubule overlaps in the spindle midzone during mitosis (Gaillard et al., 2008, Subramanian et al., 2010, Loiodice et al., 2005). Microtubule-microtubule sliding by Eg5, kinesin-1, kinesin-14 and dynein has been implicated in microtubule organisation and force generation (Straube et al., 2006, Fink, 2006, Lu et al., 2013, Kapitein et al., 2005, Braun et al., 2009, Fink et al., 2009, Tanenbaum et al., 2013) and we begin to

understand how the interplay of motors and MAPs organises particular microtubule arrangements (Bieling et al., 2010, Braun et al., 2011, Janson et al., 2007).

Here we show that the microtubule array in myoblasts is highly motile and becomes increasingly parallelised and immobilised as cells progress through the differentiation programme. We identify a previously uncharacterised differentially regulated isoform of microtubule-associated protein MAP4, called oMAP4, as a key organiser of microtubules in differentiating cells. Depletion of oMAP4 results in microtubule misalignment and increased microtubule motility in differentiating muscle cells. This results in defects in myogenic progression, cell polarisation and cell-cell fusion. We further show that oMAP4 zippers preferentially antiparallel microtubules *in vitro* and restricts motor-driven microtubule sliding in differentiating muscle cells. Based on our own data, we propose a model whereby the cooperation of motor-driven microtubule-microtubule sliding and oMAP4-mediated zippering organises the microtubule cytoskeleton in differentiating muscle cells to support and govern cell polarisation and differentiation.

RESULTS

Microtubules become progressively more ordered and immobile during muscle differentiation

To characterise microtubule organisation in differentiating muscle cells, we determined filament orientation, motility and growth characteristics of microtubules at different stages during differentiation of C2C12 cells. As reported previously, we found that microtubule organisation changes from a radial, centrosome-dominated array in undifferentiated cells, to a paraxial array in myotubes (Fig.1a) (Warren, 1974, Tassin et al., 1985). Microtubule growth directionality relative to the longitudinal axis of the cell was determined by tracking EB3-tdTomato labelled microtubule ends. The asymmetry in the distribution of microtubule growth angles increases significantly during the first two days of differentiation (Fig. 1b-d, Figure 1-figure supplement 1). This suggests that guided growth of microtubules (probably along existing microtubules) contributes to the progressively more ordered parallel microtubule array in differentiating cells. Furthermore, microtubules within the array are highly motile in undifferentiated myoblasts as visualised by photoactivation of paGFP-Tubulin or conversion of mEos2-Tubulin (Fig. 1e-f, Videos 1-2). In differentiating muscle cells, microtubules become very

stable and static as seen by the low frequency and speed of microtubule sliding movements and by diminished loss of microtubules from the photoactivated region due to depolymerisation (Fig. 1e-h, Figure 1-figure supplement 2, Video 3). The reduction in microtubule movements could be due to the differential regulation of motors that drive microtubule sliding. Conventional kinesin as well as dynein have been implicated in microtubule-microtubule sliding and microtubule movement along the cell cortex in other cell systems (Lu et al., 2013, Bicek et al., 2009, Fink, 2006, Jolly et al., 2010, Rusan et al., 2002, Straube et al., 2006, Samora et al., 2011). Both motors contribute to microtubule movements in myoblasts as the frequency of microtubule movements was reduced more than 3-fold upon depletion of either dynein heavy chain or Kif5b (Fig. 1e-h, Figure 1-figure supplement 3, Videos 4-5). However, Kif5b and dynein were continuously expressed during muscle differentiation (Fig. 1i), suggesting that other factors prevent motor-dependent microtubule sliding and promote parallel microtubule array formation during myogenesis.

Three MAP4 isoforms are expressed in differentiating muscle cells

Structural MAPs are candidates for a role in organising parallel microtubule arrays and regulating motor activity. MAP4, the only non-neuronal member of the MAP2/Tau family, has been reported to stabilise and bundle microtubules (Nguyen et al., 1997, Nguyen et al., 1998, Ookata et al., 1995, Hasan et al., 2006, West et al., 1991, Aizawa et al., 1991). Our previous finding that MAP4 can limit force generation by dynein motors (Samora et al., 2011) suggested that MAP4 might prevent dynein-driven microtubule motility in muscle cells. Mouse skeletal muscle cells express tissue-specific isoforms of MAP4 (Mangan and Olmsted, 1996). To investigate the differential regulation of experimentally confirmed and predicted MAP4 transcripts (Fig. 2a), we performed RT-PCR analysis of total RNA isolated from differentiating C2C12 cells. We confirmed the continuous expression of the ubiquitous isoform uMAP4 and upregulation of muscle-specific mMAP4 24 hours post induction of differentiation (Fig. 2b). Interestingly, we found that a previously uncharacterised isoform, with a unique 48kD projection domain, was also upregulated after 24 hours of differentiation. In addition to muscle, this isoform is also highly expressed in brain tissue (Figure 2-figure supplement 1). We refer to this isoform as oMAP4. Further analysis revealed that uMAP4, mMAP4 and oMAP4 transcripts were each expressed as variants with three, four or five tau-like microtubule binding repeats due to

alternative splicing of exons 14 and 15 (Figure 2-figure supplement 2). To confirm that these transcripts encode proteins, we generated specific antibodies for mMAP4 and oMAP4 and probed whole cell lysates of C2C12 cells on Western blots. Both, mMAP4 and oMAP4 protein levels increase between 24 and 48 hours after differentiation (Fig. 2c-d). As expected, GFP fusion proteins of uMAP4, mMAP4 and oMAP4 decorated microtubules along their length in C2C12 cells (Figure 2-figure supplement 3).

oMAP4 is required for muscle cell elongation and fusion

To investigate their involvement in microtubule organisation in muscle cells, we depleted each MAP4 isoform using a vector-based RNA interference approach. GFP-Tubulin was co-expressed with the short hairpin RNAs (shRNAs) to serve as a marker to detect successful transfection. Efficient depletion was confirmed by Western blotting of FACS-sorted GFP-positive cells and by immunofluorescence (Figure 2-figure supplements 4-5). Muscle differentiation phenotypes were assessed as (1) the ability of single nucleated cells to elongate and (2) the efficiency of cells to fuse and form syncytia containing 3 or more nuclei (Straube and Merdes, 2007). 48 hours after differentiation, the average length of myoblasts treated with control shRNA was 107±40 μm. Depletion of uMAP4 did not significantly affect this (105±36 μm, $p=0.4$; Fig. 2e-f). Depletion of mMAP4 allowed myoblasts to elongate to an average length of 143±58 μm, which is significantly longer than control cells. Myoblast fusion efficiency was not significantly affected following depletion of uMAP4 or mMAP4 (Fig. 2g). In contrast, the depletion of oMAP4 caused severe defects in myoblast elongation and fusion. oMAP4-depleted cells had an average length of 82±39μm, which is significantly shorter than control myoblasts ($p<<0.001$, Fig. 2e-f). Furthermore, cell-cell fusion efficiency was reduced more than 4-fold following depletion of oMAP4 (Fig. 2g). Importantly, co-transfection of an RNAi-resistant version of oMAP4 (FLAG-oMAP4^{RIP}) rescued the myoblast elongation and fusion defects caused by oMAP4 shRNA (Fig. 2h-i, Figure 2-figure supplement 6). The overexpression of uMAP4 was not able to rescue oMAP4-depletion phenotypes (Fig. 2i). Our data collectively demonstrate that oMAP4 is specifically required for morphogenesis and cell-cell fusion during muscle cell differentiation.

oMAP4 depletion leads to disorganised microtubules

To understand which processes in the myogenic programme depend on oMAP4, we analysed the timing of myogenic events. We find a severe delay and reduction in the expression of embryonic myosin, a structural protein required for sarcomere formation, in oMAP4-depleted cells (Fig. 3a-c). Likewise, the relocation of centrosomal proteins to the nuclear surface of myoblasts, a characteristic event during myogenesis (Srsen et al., 2009, Tassin et al., 1985), is severely delayed in oMAP4-depleted cells (Fig. 3d-e). These results confirm that progression through the myogenic differentiation programme depends on oMAP4. Previous work has shown that interference with microtubule stability and the acquisition of posttranslational modifications of tubulin result in similar myogenesis defects (Spencer et al., 2000, Zhang et al., 2009, Chang et al., 2002). Depletion of oMAP4 did not result in a reduction of tubulin acetylation (Fig. 3f), perhaps because other microtubule stabilisers were still present. Nevertheless, the microtubule cytoskeleton appeared disorganised in oMAP4-depleted cells (Fig. 3a-b). To quantitatively assess microtubule network organization and distinguish this from effects due to different morphology and differentiation status, we selected mono-nucleated elongated myoblasts treated with control and oMAP4 shRNA and manually traced GFP-Tubulin-labelled microtubules in equivalent sections of these cells (Fig. 3g, Videos 6-7). We found that the microtubule network was largely parallel in control cells with ~80% of microtubules oriented ±15º of the longitudinal cell axis. This was reduced to ~50% in oMAP4-depleted cells (Fig. 3h). Microtubule orientation was fully rescued by expression of an RNAi-resistant oMAP4 construct (Figure 3-figure supplement 1). Depletion of mMAP4 increased paraxial microtubule alignment and uMAP4 depletion slightly reduced it (Figure 3-figure supplement 1). We confirmed the microtubule alignment defect caused by oMAP4 depletion results by tracking growing microtubule ends labelled with EB3-tdTomato (Fig. 3i, Videos 8-9). While microtubule growth speed and duration were only slightly affected, the orientation of microtubule growth deviated more from the longitudinal cell axis when oMAP4 was depleted compared to control cells (Fig. 3j-l, Figure 3-figure supplement 2).

oMAP4 prevents motor-driven microtubule sliding in cells

We hypothesized that a failure in the guidance of microtubule assembly along existing filaments could be the underlying cause of the disorganised microtubule network. Alternatively, microtubule sliding

and looping as observed in undifferentiated cells could disorganise the microtubule network in oMAP4-depleted cells. To distinguish between these possibilities we analysed microtubule motility in differentiated, shRNA-treated cells, again selecting elongated, mono-nucleated cells to exclude effects due to morphology alone. As described above, microtubule motility was strongly suppressed in differentiating muscle cells (Fig. 1e-h, 4a). Depletion of oMAP4 resulted in a more than 4-fold increase in the frequency of microtubule sliding events and these were significantly faster than those in control cells (Fig. 4a-d). In addition, the rare sliding events in differentiated control cells were usually restricted to movements parallel to the long axis of the cell, while microtubules were observed to loop in oMAP4 depleted cells, similarly to undifferentiated cells (Fig. 4e, Videos 1-3,10-11). These observations suggest that oMAP4 acts to maintain the parallel microtubule network by restricting microtubule movement, especially those that are off-axis.

As we demonstrated in a previous study that uMAP4 limits force generation by dynein to prevent excessive movement of astral microtubules along the cell cortex (Samora et al., 2011), we wondered whether oMAP4 prevents microtubule sliding by inhibiting dynein function directly or whether oMAP4 crosslinks microtubules and acts as a brake to all motor-driven sliding. In order to distinguish between these possibilities, we co-depleted dynein from oMAP4-depleted cells. If oMAP4 would act exclusively through dynein, we posited this should rescue the depletion phenotypes. Depletion of dynein heavy chain alone did not significantly affect the already low microtubule sliding frequencies in differentiated cells, although the velocity of microtubule sliding was reduced (Fig. 4b-d). Cells co-depleted for dynein and oMAP4 still showed a high frequency of microtubule sliding events (Fig. 4b-c), although fast sliding events and looping were reduced (Fig. 4d-e). Consequently, dynein co-depletion slightly alleviated the microtubule disorganisation caused by oMAP4 depletion, but did not fully rescue it (Figure 4-figure supplement 1). These results suggest that oMAP4 prevents microtubule sliding by crosslinking microtubules rather than by inhibiting dynein force generation per se. Indeed, expression of GFP-oMAP4 in undifferentiated myoblasts resulted in a significant increase in strong microtubule bundles, while expression of GFP-uMAP4 had no effect (Fig. 4f-g).

oMAP4 crosslinks antiparallel microtubules *in vitro*

To directly test the hypothesis that oMAP4 is a crosslinker, we recombinantly expressed and purified oMAP4 and GFP-oMAP4 from *E. coli* (Fig. 5a). Using *in vitro* microtubule co-sedimentation assays, we confirmed microtubule-binding activity of the purified proteins (Fig. 5b). When Taxol- or GMP-CPP-stabilised microtubules were incubated with 60nM oMAP4, we frequently observed microtubule bundles and structures with crossovers (Fig. 5c-f). This confirmed that oMAP4 has microtubule crosslinking activity. We next asked whether oMAP4 has the ability to organise dynamic microtubules into antiparallel bundles *in vitro*. To do this, we used total internal reflection (TIRF) microscopy to visualise microtubules assembled from biotinylated microtubule seeds immobilised on streptavidin-coated coverslips. In control chambers, microtubules continued growing without changing direction when they encountered other microtubules and microtubules only overlapped when they happened to grow in the same direction (Fig. 6a-b, Video 12). The addition of GFP-oMAP4 promoted zippering of those growing microtubules that encountered each other at shallow angles (Fig. 6a-c; Video 13). To assess whether oMAP4 was specific for the orientation of the microtubules, we determined microtubule polarity based on the growth characteristics of the microtubule ends observed in the Video (Fig. 6c) and determined the rate of microtubule zippering relative to the incident angle of the two microtubules. No microtubule zippering events were observed at angles between 25º and 150º, suggesting that oMAP4 can only generate forces to bend microtubules by up to 30º. Furthermore, oMAP4 showed a strong preference for zippering antiparallel oriented microtubules (Fig. 6b-c).

Another known antiparallel microtubule bundling protein, PRC1 is a dimer that accumulates specifically in antiparallel microtubule overlaps in the spindle midzone (Subramanian et al., 2010). We observed that PRC1 was more potent to bundle stabilised microtubules free in solution than oMAP4 (Fig. 5e-f). However, PRC1 was not able to zipper microtubules in our assays using dynamic microtubules growing from immobilised seeds (Fig. 6b). This is in agreement with the literature that described PRC1 to specifically bind to antiparallel microtubule overlaps that form when microtubules "occasionally encountered each other in a plus end-to-plus end configuration" (Bieling et al., 2010) rather than PRC1 itself causing the formation of the overlaps. We do not observe a substantial enrichment of GFP-oMAP4 in antiparallel or parallel overlaps (Fig. 6c). To determine whether the bias in zippering towards antiparallel oriented microtubules could be due to differences in the length of microtubules that encountered each other, we measured the length dependence of MAP4-mediated zippering. We found similar distributions of microtubule lengths for encounters that resulted in

zippering and those encounters that occurred at similarly shallow incipient angles but not led to zippering (p=0.22). Likewise, there was no difference between parallel and antiparallel encounters that were zippered (p = 0.59) and those that did not result in zippering (p=0.88) (Figure 6-figure supplement 1). Therefore, our results demonstrate that oMAP4 is a microtubule organising factor, which can arrange microtubules into antiparallel and with lesser efficiency parallel bundles. This function is consistent with the depletion phenotypes observed in differentiating muscle cells, where oMAP4 helps to arrange paraxial microtubules and thereby supports cell differentiation.

oMAP4 bundles withstand motor forces

PRC-1 is dimer that forms highly ordered crosslinks that do not substantially limit microtubule-microtubule sliding at moderate concentrations (Subramanian et al., 2010). As we proposed that oMAP4 contributes to microtubule alignment by preventing microtubule sliding in differentiating muscle cells, we next asked how oMAP4 crosslinks microtubules and whether these can withstand motor forces. We considered whether the unique projection domain in oMAP4 confers microtubule crosslinking activity by dimerisation. Proteins of the MAP2/tau family are highly elongated, structurally disordered monomers (Devred et al., 2004, Hernandez et al., 1986). Using the GOR secondary structure prediction method, we find that oMAP4, uMAP4 and tau share a similar structure of over 60% random coil, about 20% helical and 13% extended strand (Garnier et al., 1996). Furthermore, no significant coiled-coil domain was predicted. To confirm this, we performed sedimentation analysis of bacterially expressed oMAP4 and GFP-oMAP4 in comparison with a number of standard proteins (Fig. 6d,e). We obtained sedimentation constants of 3.6±0.25 S and 4.3±0.21 S, respectively. Given the molecular weight of the monomers being 99kD and 131kD, respectively, we can calculate the frictional ratio f/f_{min}=2.1, suggesting that oMAP4 is a highly elongated monomer with a shape comparable to tau (f/f_{min}=1.8, (Devred et al., 2004)). We therefore predict that oMAP4 most likely bundles microtubules using a second microtubule-binding region in its projection domain.

Single kinesin-1 and dynein molecules can generate forces of up to 7pN (Nishiyama et al., 2002, Toba et al., 2006). To determine whether oMAP4 bundling can indeed withstand the forces exerted by several motors tugging the microtubules apart, we performed gliding assays with kinesin-1. The presence of 80nM oMAP4 did only slightly affect the velocity of kinesin-mediated movements of single

microtubules (Fig. 7a-b). However, antiparallel microtubule bundles formed in solution and landing on the kinesin surface were often static or their movement was slow and non-persistent (Fig. 7c-e, Video 14). Given their predominantly antiparallel arrangement, forces on the microtubules within a bundle would cancel each other out as long as the linkage between the microtubules is maintained. Occasionally, bundles were driven apart. This usually occurred in bundles where extensive lateral forces were generated on one microtubule that was significantly longer than other microtubules in the bundle (Fig. 7c). The antiparallel nature of the oMAP4-generated bundles was confirmed in these cases from the opposing direction of their movement after separation (Fig. 7c, magenta arrows). Most importantly, we observed that more than 75% of microtubule bundles withstand motor forces for the entire duration of our 7.5min Videos (Fig. 7c,e,f, yellow arrows), suggesting that oMAP4-mediated cross-linking is indeed able to prevent motor-driven microtubule sliding as we hypothesised.

DISCUSSION

Why is a highly organised microtubule cytoskeleton required to undergo muscle differentiation? Microtubules are the stiffest of the cytoskeletal polymers that can bear high compressive loads, especially when reinforced laterally (Brangwynne et al., 2006). Our data support a model in which microtubules fulfil a structural role during the elongation of muscle cells. If so, one would expect that the degree of alignment of microtubules will correlate with a cell's ability to elongate. We tested this by plotting the Kuiper statistic as a measure of microtubule orderliness against the mean cell length of 48 hours differentiated cells for different RNAi treatments used in this study and found indeed a linear correlation (Fig. 8a). Likewise, the depletion of mMAP4, which increases the length of differentiating myoblasts also increases the paraxial microtubule alignment beyond that of control cells (Figure 3-figure supplement 1). These data support the idea that MT orientation is strongly linked to the morphological changes required for muscle differentiation. As observed for oMAP4, our previously published data on EB3 depletion (Straube and Merdes, 2007) and a number of unpublished observations, myoblasts that fail to elongate are also impaired in cell-cell fusion. While we don't yet understand the relationship between cell elongation and fusion, a mechanism to prevent the fusion of myoblasts that did not complete the previous step of differentiation, makes intuitively sense. oMAP4 depleted cells show in addition to impaired morphological changes, also a delay in the expression of

myogenic markers such as myogenin and embryonic myosin, further suggesting that a signalling step in the differentiation programme has not been completed. Microtubules have been implicated in a signalling role during myogenesis based on the observation that altering the level of posttranslational tubulin modifications either through chemical inhibition or depletion of microtubule-stabilising MAPs leads to similar delays in the expression of differentiation markers and impaired formation of myotubes (Chang et al., 2002, Spencer et al., 2000, Zhang et al., 2009). The depletion of oMAP4 does not negatively affect tubulin acetylation (Fig. 3f) but might impact other aspects of this putative microtubule-dependent signalling event. It will be a future challenge to elucidate the pathway that couples microtubule organisation and chemical modification to the timing of the myogenic protein expression programme.

We show that oMAP4 and PRC1 are both microtubule bundling proteins, but with very different properties. While PRC1 is an antiparallel dimer that forms ordered crosslinks of a defined distance and specifically enriches in antiparallel microtubule overlaps (Bieling et al., 2010, Subramanian et al., 2010), oMAP4 has little preference for binding to bundles, but instead is able to zipper microtubules. Zippering of microtubules growing from surface-attached seeds requires bending of microtubules. We consider that the lateral forces required to bring two microtubules close together against the rigidity of the microtubule have to be borne by a single crosslinking molecule. Thus our data suggest that single molecules of oMAP4 can resist higher loads than PRC1 crosslinks. When we apply longitudinal forces as experienced by pre-formed bundles in kinesin gliding assays, the shear forces are probably shared between several crosslinking molecules thus enabling oMAP4 to withstand counteracting motor forces on the bundled microtubules. Bundles that contain one very long microtubule that is driven laterally on the kinesin surface, eventually splay apart as lateral forces cannot be shared between the crosslinkers. In contrast, PRC1 cannot resist motor forces and at moderate levels only slightly slows motor-driven sliding of microtubules (Bieling et al., 2010, Subramanian et al., 2010). Thus oMAP4 has the required properties to fulfil the role of a microtubule organiser, justifying its name as organising microtubule-associated protein 4, although the structural basis for oMAP4's antiparallel zippering remains to be elucidated.

The motors dynein and kinesin move microtubules and cause apparent disorder that is limited by oMAP4 crosslinking. However, both motors have also been reported to bundle and organise

316 microtubules. Indeed, dynein depletion alone results in reduced microtubule alignment (Figure 4-
317 figure supplement 1). This is consistent with the finding that dynein controls muscle length in
318 *Drosophila* (Folker et al., 2012) and earlier reports of dynein involvement in the self-organisation of
319 microtubule networks and its ability to crosslink and slide antiparallel microtubules as well as
320 transporting microtubules along the cell cortex (Adames and Cooper, 2000, Fink, 2006, Heald et al.,
321 1996, Merdes et al., 2000, Tanenbaum et al., 2013, Samora et al., 2011). As oMAP4 is only able to
322 efficiently zipper microtubules at incident angles of less than 30º if antiparallel and less than 10º if
323 parallel, we propose that dynein-mediated looping and buckling of microtubules (Fig. 4e, (Fink, 2006,
324 Tanenbaum et al., 2013)) brings microtubules into a favourable position for oMAP4-mediated
325 zippering. As oMAP4-mediated bundling resists motor-driven sliding, dynein can only move those
326 microtubules that are not yet aligned to the paraxial network. Thus dynein and oMAP4 are likely to
327 cooperate in the formation of the highly ordered microtubule arrangement in differentiating muscle
328 cells (Fig. 8c). In the absence of oMAP4, excessive motor-driven microtubule motility disorganises
329 microtubules. In the absence of dynein, oMAP4 might stabilise high-angle microtubule crossovers, but
330 will not be able to align them into the network. If the activity of both oMAP4 and dynein is reduced,
331 oMAP4 zippering is missing and kinesin-mediated sliding and bundling (Jolly et al., 2010, Straube et
332 al., 2006) prevails (Fig. 8b). In agreement with this model, some disorganisation of microtubules has
333 been observed in kinesin-1-depleted myotubes (Wilson and Holzbaur, 2012). Microtubule-microtubule
334 sliding has recently been implicated in driving neurite outgrowth (Lu et al., 2013) and paraxial
335 microtubule arrangements have been shown to drive dorsal closure during embryonic development
336 (Jankovics and Brunner, 2006). Thus the mechanisms we reveal here for motor and MAP cooperation
337 in the formation of paraxial microtubule networks are likely to be of importance beyond muscle cells.
338 Indeed oMAP4 is highly expressed in brain (Figure 2-figure supplement 1), suggesting that it might be
339 required to support the paraxial microtubule arrays in dendrites and the axon.

340 While the zippering model described above explains how an paraxial array is maintained in the
341 presence of microtubule turnover, it does not explain how the symmetry of the radial microtubule
342 cytoskeleton in the myoblast is broken in the first place. We think that a bipolar elongating myoblast
343 can be compared to a migrating cell with two fronts. Symmetry breaking in cell migration occurs
344 through protrusion mediated by the actin cytoskeleton. Microtubules support and stabilise cell
345 protrusions and microtubule plus ends are selectively stabilised at the leading edge (Waterman-Storer

et al., 1999, Kaverina and Straube, 2011). This establishes and reinforces the new polarity axis. Similarly, in differentiating myoblasts dynamic capture of microtubule plus ends occurs at the cell tips (Straube and Merdes, 2007). This leads to the selective stabilisation of paraxial microtubules to break the symmetry in the microtubule network. The zippering mechanism described here would promote shorter microtubules to align to longer and already bundled microtubules and thus amplify the directional bias and increase stability and orderliness in the paraxial array. It is likely that the guidance of microtubule growth through the cooperation of plus end tracking proteins and motors also contributes to maintenance of the ordered array (Mattie et al., 2010). It will be interesting to dissect the contributions of these different pathways to microtubule network reorganisation, not only at the onset of myogenesis, but also during later stages when the parallel network is replaced by the grid-like lattice found in adult muscle (Oddoux et al., 2013).

METHODS

RNA Extraction, cDNA Preparation and Gene Expression Analyses

RNA was extracted from 0-60 hrs differentiated C2C12 cells using Trizol reagent (Invitrogen) and random-primed cDNA was synthesized using RevertAid H Minus M-MuLV reverse transcriptase (Fermentas) according to manufacturer's protocol. PCR reactions were carried out using cDNA timecourse samples as templates, isoform-specific upstream primers GCCAGCCTTCTGAGCCTTG (for uMAP4), GAGATCCAAGATGTTCAAGTC (for mMAP4) and CTGTTGGAAGAGACCCCAC (for oMAP4) and downstream primers CAGCTGGCACTGAGCCTG (to determine relative expression levels) and GAAGGGCCTCACTGCCAC (to determine number of microtubule binding repeats). As control, the coding sequence of Glyceraldehyde-3-Phosphate Dehydrogenase (GAPDH) was amplified using the primers CCCACTTGAAGGGTGGAG and CAGGCGGCACGTCAGATC.

For differential expression analyses of MAP4 isoforms, the mouse genome assembly (release date July 2007 (NCBI37/mm9) was examined using the UCSC Genome Browser at http://genome.ucsc.edu/. For RNA sequencing analyses, raw data from previously described C2C12 datasets ((Trapnell et al., 2010), see supplementary files) of the Mouse ENCODE project were exported. Reads Per Million (RPM) values were then summed and divided by the length of sequenced regions to obtain RPM/Kb values. Expression levels of MAP4 isoforms in various tissues were

compared by exporting and analysing published Affymetrix mouse exon array datasets (see supplementary data; (Pohl et al., 2009), see supplementary files) from the Genome Browser.

Cloning of MAP4 isoforms, shRNA plasmids, mammalian and bacterial expression constructs

For cloning uMAP4 (accession number M72414) and oMAP4 (accession number BC042645), cDNA was amplified using primers CAGGTCGACAGAATGGCCGACCTCAG and GACCGCGGACGAGACCAGAATGTCATC for uMAP4, and GAGGTCGACATGGACTCCCGGAAAGAAATC and CCCGCGGTCTCAATTTGTCTCCTGG for oMAP4. PCR products were cloned into the MscI site of pCAP^{s} (Roche) and confirmed by sequencing, digested with SalI and SacII and transferred into pEGFP-C1 (Clontech). To clone mMAP4 (assembled from sequences under accession numbers M72414 and U08819), two overlapping fragments encoding its N-terminal and C-terminal domains were generated by PCR using primers CAGGTCGACAGAATGGCCGACCTCAG and CTGCAATCAGCAAGCCCAC, and CCTCTGGGAGATCACCATC and CCCGCGGTCTCAATTTGTCTCCTGG respectively and each cloned into pCAP^{s} and sequenced. Plasmids carrying N-terminal and C-terminal coding sequences were then digested with SalI+SpeI and SpeI+SacII respectively and cloned into the SalI+SacII sites of pEGFP-C1. To clone FLAG-oMAP4, a 5X-FLAG tag (DYKDADLDKDDDDK) was amplified by PCR and digested with NgoMIV and SalI. It was then inserted into pEGFP-oMAP4 that was opened with AgeI and SalI, thereby replacing the eGFP ORF. FLAG-oMAP4^{RIP} was generated using FLAG-oMAP4 as a template and primers GAGGTCGACATGGACTCCCGGAAAGAAATC, CTCCTCGAGTTAAGCAGTTGGTACCTGAG and CCCAGCTGTGAACTTGGTTGATAAGTACCCCTG in 3-step mutagenesis PCR.

Bacterial expression vector for N-terminally 6xHis-tagged oMAP4 was generated by SalI+MfeI digestion of pEGFP-oMAP4 (four MTB repeats) and insertion of the coding sequence into the XhoI+EcoRI sites of pRSET-A. N-terminally 6x-His-eGFP-tagged oMAP4 expression construct was cloned by transferring EGFP-oMAP4 with NcoI-MfeI from pEGFP-oMAP4 (five MTB repeats) into the NcoI-EcoRI sites of pRSET-B vector (Invitrogen).

To clone GST fusions of MAP4 fragments for polyclonal antibody generation, regions specific to mMAP4 (amino acids 631-1,060) and oMAP4 (amino acids 22-350) were obtained by PCR using pEGFP-mMAP4 (primers GCCAGCCTTCTGAGCCTTG and

CTCCTCGAGTTAAGTAATGGCCCCTGGTTG) and pEGFP-oMAP4 (primers GAGGGTCAATTGAATGAAATCGGGCTGAATG and CTCCTCGAGTTAAGCAGTTGGTACCTGAG). mMAP4 and oMAP4 PCR products were then digested with EcoRI+XhoI and MfeI+XhoI respectively and inserted into the EcoRI+XhoI sites pGEX-6P-1 vector (GE healthcare).

Depletion constructs were based on pSUPERneo.gfp (Oligoengine). shRNA target sequences were chosen using Oligo Retriever (http://cancan.cshl.edu/RNAi_central/RNAi.cgi?type=shRNA) and were as follows: shControl (targeting Luciferase): CGTACGCGGAATACTTCGA; sh-uMAP4: GCCTTGCTCAGGAGTATCC; sh-mMAP4: CAGAGAGTTTGGATAAGAA; sh-oMAP4: GCTGTGAATCTTGTCGATAAG; shDHC: CAATTACAGTCTGGAGTTA; shKHC (targeting Kif5b):CAATTGGAGTTATAGGAAA. The neo.gfp cassette was replaced by GFP-Tubulin, mCherry-Tubulin or mEos2-Tubulin.

EB3-tdTomato, paGFP-Tubulin and mEos2-Tubulin were described previously (McKinney et al., 2009, Samora et al., 2011, Rusan, 2004).

Generation and purification of polyclonal Antibodies

Rabbit polyclonal antibodies against specific regions in oMAP4 and mMAP4 were raised against affinity purified GST-oMAP4$_{22\text{-}350}$ and GST-mMAP4$_{631\text{-}1060}$ respectively by Absea Biotechnology Ltd. Polyclonal antibodies were purified from sera using the same GST fusion proteins. To do this, purified protein samples were run on SDS-PAGE, transferred to nitrocellulose membranes, protein bands were stained with Ponceau S and excised using a sterile scalpel. Membrane pieces were blocked with 5% w/v milk in TBST, cut into small pieces and incubated over night at 4°C in 1ml TBST and 1ml antiserum. Membrane pieces were washed thrice with TBST and antibodies were eluted by adding 200µl 100mM Glycine-HCl (pH 2.5) and vortexing for 1 min. Purified antibodies were then transferred to fresh tubes and neutralized immediately by adding 10µl 1M Tris-Base. Antibodies were stored at -20°C after adding Glycerol to a final concentration of 50% v/v.

Cell culture, plasmid transfections, and myoblast differentiation

Mouse C2C12 myoblasts were cultured on rat tail collagen (Sigma) in DMEM-GlutaMAX (Invitrogen) supplemented with 10% fetal bovine serum (FBS), 2mM L-Glutamine, 100U/ml penicillin and

100µg/ml streptomycin with 5% CO_2 in a humidified incubator. For localization analyses, myoblasts were transfected with 1µg plasmid DNA using Fugene 6 reagent (Roche) and analysed 48 hours post-transfection. For myoblast elongation and fusion analysis, 10,000 or 20,000 C2C12 cells respectively were seeded onto collagen coated coverslips. Cells were transfected 24 hours later with a total amount of 1.5µg shRNA constructs or shRNA and rescue constructs using Lipofectamine Plus reagent (Invitrogen) in OptiMEM (Invitrogen), which was replaced with growth medium 4-6 hours after transfection. Muscle cell differentiation was induced by replacing growth medium with differentiation medium (DMEM, 0.1% FBS, 2mM L-glutamine, 5µg/ml insulin, 5µg/ml, transferrin, 100U/ml penicillin and 100µg/ml streptomycin) 20 hrs after shRNA transfection. Differentiation medium was changed daily and analysis of shRNA transfected cells was consistently performed 72–78 hr after transfection.

Live cell imaging and immunofluorescence experiments

Live cells were imaged at 37°C and 5% CO_2 in a stage top incubator (Tokai Hit) using a 100x or a 60x oil NA 1.4 objective on a Deltavision system (Applied Precision, LLC) using Chroma filter sets and a Coolsnap HQ camera controlled by SoftWorx (Applied Precision, LLC). For all analysis of microtubule phenotypes, mono-nucleated, elongated cells were selected. For analyses of microtubule dynamics during myoblast differentiation, fluorescence images of EB3-tdTomato were acquired with 500ms exposure at a temporal resolution of 3s for 120s. EB comets were tracked using plusTipTracker and further analysed for microtubule directionality using custom MATLAB code (see supplementary file MTdirectionality.m). For microtubule motility experiments, cells were transiently transfected with pSuper-mEOS2-Tubulin plasmids or co-transfected with paGFP-Tubulin and pSuper-mCherry-Tubulin plasmids. The microtubule cytoskeleton was focussed and bar-shapes regions of interest perpendicular to the microtubule network were selected using the non-converted mEOS2-Tubulin or mCherry-Tubulin signal. After photoactivation or -conversion of these regions of interest using 10% 406nm with the Deltavision photokinetics module laser power, images were acquired with 500ms exposure at a temporal resolution of 1.6s per frame for 60s or lower temporal resolution for up to 6 minutes. Images were deconvolved with low noise filtering method for 10 iterations using SoftWorx (Applied Precision, LLC). Microtubule motility events were scored when an activated fragment moved for more than 0.5µm from its original location. The velocity of microtubule movements was determined as the average velocity during each motility event, which lasted on average 15-20 s. Directionality of

464 microtubule motility was scored as paraxial if within 45º of the long axis of the cell. Looping
465 microtubules were defined as those that underwent a directional change of more than 90º during the
466 movement event. For analysis of the contribution of microtubule dynamics and motor-driven
467 microtubule movement to microtubule loss from photoactivated regions, undifferentiated or 48hrs
468 differentiated C2C12 cells expressing mEOS2-Tubulin were treated with either 10μM Taxol (to
469 suppress MT depolymerisation) or 5mM azide in 1mM 2-deoxyglucose (to suppress motor activity) or
470 a mixture of Taxol and azide (as a control for photobleaching) for 30 mins before imaging. Signal
471 intensity of photoconverted regions at each time point recorded using ImageJ. After background
472 subtraction, photobleaching correction and normalization of fluorescence intensity, the half-life of
473 signal dissipation was determined by fitting a single exponential curve to the fluorescence intensity
474 data over time.
475 For immunofluorescence experiments, cells were fixed in -20°C cold methanol for 24-48 hours. Fixed
476 cells were rehydrated by washing with PBS for 5 min and blocked with 0.5% BSA w/v in PBST for 5
477 min. Coverslips were then incubated with primary antibodies overnight at 4°C or for 4 hours at RT and
478 secondary antibodies for 1 hour in 0.5% BSA w/v in PBST. To stain DNA, coverslips were incubated
479 with 4′,6-Diamidino-2-phenylindole dihydrochloride (DAPI; Sigma #D9542) for 2 min. Coverslips were
480 then mounted using Vectashield mounting medium (Vector Labs #H-1000). Primary antibody dilutions
481 were as follows: rabbit anti-mMAP4 (1:1,000), rabbit anti-PCM-1 (1:500, (Dammermann and Merdes,
482 2002)), mouse anti-embryonic myosin (1:50; F1.652, DSHB), mouse anti-α-tubulin (1:1,000; DM1A,
483 Sigma), mouse anti-acetylated tubulin (1:1,000; 6-11B-1, Sigma), mouse anti-myogenin (1:50; F5D,
484 Santa Cruz). Alexa488-, Alexa594- or Alexa647-conjugated anti-mouse or anti-rabbit secondary
485 antibodies (Molecular Probes) were used at 1:500 dilution. For myoblast elongation analysis, cells
486 were imaged using a 20x objective on the Deltavision system as above. Cell lengths of GFP-Tubulin-
487 positive mono-nucleated cells were measured as straight-line distance from tip-to-tip using Image-Pro
488 Analyzer 7.0 (Media Cybernetics). For cell fusion analysis, cells with two or less nuclei (visualised as
489 holes in GFP-Tubulin signal) and those with 3 or more nuclei were counted on the entire coverslip
490 directly on the Deltavision microscope using a 20x objective and GFP filter sets. To analyse
491 microtubule filament arrangement, GFP-Tubulin was imaged on a Perkin-Elmer UltraView spinning
492 disk confocal system using a 488nm laser and an Orca-R2 camera (Hamamatsu) under the control of
493 Volocity software (Perkin-Elmer). Filaments were manually traced using ImageJ and deviation from

494 the longitudinal cell axis calculated in MATLAB. To determine the number of bundles per cell,
495 undifferentiated C2C12 cells were transiently transfected with either GFP-oMAP4 or GFP-uMAP4,
496 fixed after 24 hours and stained with tubulin antibodies. Bundles were scored when elongated regions
497 of more than 2.3µm length had an intensity of more than three-fold of a single microtubule.
498 Superresolution images of microtubules labelled with anti-tubulin and Alexa488-conjugated anti-
499 mouse antibodies and embedded in ProLong Gold reagent (Molecular Probes) were obtained on a N-
500 SIM system (Nikon) at The Babraham Institute using 3D SIM mode with 15 individual images
501 collected for reconstruction.
502

503 **Immunoblotting**

504 For validation of depletion, shRNA-transfected and 52-54 hrs differentiated cells were detached from
505 culture dishes with Trypsin- EDTA. Trypsinised cells were then transferred to PBS + 2% FBS and
506 GFP expressing cells were sorted on FACSDiva or Influx instruments (BD Biosciences). Collected
507 cells were gently pelleted at 300xg for 2min, resuspended to 10,000 cells/µl in 1x sample buffer and
508 incubated at 95°C for 5min. Immunoblotting was performed as described previously (Samora et al.,
509 2011). Primary antibody dilutions were as follows: mouse anti-α-tubulin (1:10,000; DM1A, Sigma),
510 mouse anti-FLAG (1:5000; FLAG-M2, Sigma), mouse anti-DHC (1:500; R-325, Santa Cruz), mouse
511 anti-uKHC (1:750; H-50, Santa Cruz), rabbit anti-uMAP4 (1:1,000, H-300, Santa Cruz), rabbit anti-
512 mMAP4 (1:5,000), rabbit anti-oMAP4 (1:5,000), mouse anti-pentahis (1:3000, Qiagen). Horseradish
513 peroxidase (HRP) conjugated anti-mouse or anti-rabbit secondary antibodies (Promega) were used at
514 1:4,000 dilution.

515

516 **Protein purification and glycerol gradients**

517 6xHis-oMAP4 and 6xHis-GFP-oMAP4 were expressed in *E. coli* strain BL21-CodonPlus-(DE3) and
518 expression was induced with 0.5mM isopropyl-β-D-thiogalactoside at 37°C. Bacteria were lysed in
519 binding buffer (50mM NaPO4 buffer, pH 8.0; 300mM NaCl; 2mM β-mercaptoethanol; 15% glycerol) by
520 sonication. oMAP4 was bound to Ni-NTA resin (Qiagen) and eluted with 250mM imidazole in binding
521 buffer. After two-fold dilution with low-salt buffer (20mM MES, pH 6.8; 1mM EGTA; 0.5mM MgCl2) the
522 MAP4-containing fractions were loaded on SP Fast Flow Sepharose (GE Healthcare), washed with

low-salt buffer and eluted with a step gradient of high-salt buffer (20mM MES, pH 6.8; 1mM EGTA; 0.5mM $MgCl_2$; 1M NaCl). All purification was carried out at room temperature to minimize protein aggregation. Proteins were analysed by SDS–polyacrylamide gel electrophoresis and SimplyBlue staining (Invitrogen). Buffer exchange to BRB80 (80mM PIPES, pH 6.8; 1mM MgCl2; 1mM EGTA) was carried out using Vivaspin spin columns (Sartorius) according to the manufacturer's protocol. GST fusion proteins for antibody generation and purification were bound to Glutathione-Agarose (Sigma), washed with PBS and eluted with GST elution buffer (50mM Tris-HCl, pH-8.0; 150mM NaCl; 2mM 2-Mercaptoethanol; 10 mM Glutathione). Full length *Drosphila* kinesin-1 was purified previously (Braun et al., 2009). EB1-GFP-6xHis was purified as described previously (Grimaldi et al., 2014). 6xHis-PRC1 was purified using Ni-NTA as described for 6xHis-oMAP4 above.

To determine sedimentation properties, cleared extracts of BL21 cells expressing 6xHis-oMAP4 and 6xHis-GFP-oMAP4 in BRB80 plus complete protease inhibotors (Roche) were loaded onto 5ml 10-40% v/v glycerol gradients prepared with a Gradient Master (Biocomp) and spun at 45,000 xg in a SW55Ti rotor for 14 hours. Standard proteins were loaded at 5mg/ml individually on separate gradients. Gradients were fractionated by pipetting from the top in 250µl aliquots and analysed by measuring the absorbance at 280nm or analysing band intensity on coomassie-stained polyacrylamide gels or immunoblots using pentahis antibodies (Qiagen). The frictional ratio was determined $f/f_{min} = S_{max}/S$ with $S_{max} = 0.00361 \cdot M^{2/3}$ in Svedbergs for a protein of mass M in Daltons (Erickson, 2009).

In vitro microtubule zippering and kinesin gliding assays

Tubulin was prepared from pig brains according to published protocols (Gell et al., 2011). Labelled tubulin was from Cytoskleleton Inc, nucleotides were from Jena Biosciences and all other chemicals were from Sigma unless indicated. Microtubule seeds were assembled from tubulin, biotin-tubulin and Hilyte647-tubulin at a molar ratio of 25:1:2 in the presence of 1mM GMP-CPP in MRB80 (80mM PIPES, pH 6.8 with KOH, 1mM EGTA, 4mM $MgCl_2$) for 1 hr at 37ºC, diluted 20-fold with MRB80 + 2µM Paclitaxel and stored at RT. A 100µm deep flow chamber was made from a slide and a hydrochloric acid-treated coverslip using double-sided tape (Scotch 3M). For MT dynamics assays, the flow chamber was passivated with PLL-PEG-50%biotin (Susos AG, Zurich). Seeds were attached to this surface using streptavidin and blocked with 1mg/ml κ-casein. A reaction mix containing 15µM

tubulin, 1μM X-Rhodamine tubulin, 50mM KCl, 1mM GTP, 0.6mg/ml κ-casein, 0.2% methyl cellulose, 4mM DTT, 0.2mg/ml catalase, 0.4mg/ml glucose oxidase, 50mM glucose in MRB80, supplemented with 80nM GFP-oMAP4 or buffer was clarified for 8 min at 190,000xg in an airfuge (Beckman), the supernatant added to the flow chamber and sealed with candle wax. For gliding assays, 3nM Drosophila kinesin in MRB80, supplemented with 10mM β-Mercaptoethanol and 0.1mM MgATP were flown into the glass chamber, before blocking with 1 mg/ml κ-casein. The gliding mix containing X-rhodamine- and Hilyte647-labelled microtubules, 1mM ATP, 4mM $MgCl_2$, oxygen scavenger system (4mM DTT, 0.2mg/ml catalase, 0.4mg/ml glucose oxidase, 50mM glucose), ATP regeneration system (5mM phosphocreatine, 7U/ml creatine phosphokinase), 80nM GFP-oMAP4 in MRB80 was added to the flow chamber and sealed with candle wax. Microtubule assembly and gliding assays were observed on an Olympus TIRF system using a 100x NA 1.49 objective, 1.6x additional magnification, 488nm, 561nm and 640nm laser lines, a Hamamatsu ImageEM-1k back-illuminated EM-CCD camera under the control of xcellence software (Olympus). Microtubule gliding speeds were determined from tracks obtained using ImageJ plugin MTrackJ. Microtubule encounters were classified as zippering when they resulted in bundling for a minimum length of 2μm away from the initial point of contact. For parallel bundling, zippering would need to occur towards the minus end of both microtubules. For antiparallel zippering, both aligned microtubule ends would need to continue growth for at least 2μm along the lattice of the other microtubule. Microtubule lengths were measured to address whether the bias in microtubule zippering by oMAP4 arises from differences in lengths between parallel and antiparallel microtubules. For microtubule encounters in either orientation that resulted in successful zippering, distance from the point of encounter to the microtubule seed or to the next microtubule crossover point was measured. Microtubule lengths were measured similarly for unsuccessful encounters but these were restricted to shallow angle encounters at which oMAP4-mediated zippering typically occurs, i.e. 10°-30°.

Microtubule pelleting and bundling assays

Microtubules were polymerised in BRB80 buffer from 40-50 μM pig-brain tubulin in the presence of 1 mM GTP by incubation at 37°C for 30 minutes and stabilised by addition of 20μM Paclitaxel (Sigma). To remove non-polymerised tubulin, microtubules were pelleted by centrifugation at 45,000 RPM for

25 min at 27°C, washed with and resuspended in BRB80 and 20μM Paclitaxel. To test binding of MAP4 proteins to microtubules, 1.5μM of Taxol-stabilised microtubules were mixed with purified 60nM oMAP4 in the presence of 20μM Paclitaxel in BRB80 in a total volume of 50μl. Reactions were then incubated for 20 min at 37ºC and centrifuged at 35ºC, 50,000 RPM for 15 min. After recovery of the supernatant, the pellet was washed with and then resuspended in 50μl BRB80 and 20μM Paclitaxel. After addition of SDS-PAGE sample buffer, pellet and supernatant fractions were analysed by SDS-PAGE. For microtubule bundling experiments, 40μl drops of 0.1 mg/ml Poly-L-Lysine (Sigma) were placed onto 70% ethanol washed and air-dried 22x22mm glass coverslips (Menzel-Gläser). After removal of the Poly-L-Lysine solution using a bench top coverslip centrifuge (Technical Video), coverslips were rinsed three times with 150μl ddH_2O using the same procedure and air dried. To test if oMAP4 can bundle microtubules, Rhodamine-labelled microtubule seeds stabilised with GMP-CPP or Taxol-stabilised microtubules were mixed in BRB80 in a total volume of 10μl and incubated with buffer or with 60nM oMAP4 at 22°C for 10-15 min. 1μl samples of reactions were then placed onto slides, mounted with Poly-L-Lysine coated coverslips and imaged using the Deltavision widefield system as above. For comparative analysis of EB1, PRC1 and oMAP4-mediated bundling, freshly polymerised GMPCPP-stabilised Hilyte647-labelled microtubules were incubated with 80nM protein in MRB80 for 10min before loading into a 10μm flow chamber made from a slide and a poly-lysine-coated coverslip. At least 30 random fields were imaged using TIRF microscopy at critical angle. Bundles were counted if at least three times as bright as single microtubules.

Statistical data analysis

Statistical data analyses and graphing were performed using Origin Pro 8.5 (OriginLab) or MATLAB (Mathworks). Image preparation for publication was done using deconvolution in Softworx (Applied Precision), ImageJ and Adobe Illustrator. All statistical significance analyses were carried out using two-tailed two-sample t-tests assuming equal variance. Kuiper statistics was calculated from cumulative distributions of data compared to a random distribution using custom MATLAB code (see source code 1 MTdirectionality.m).

AUTHOR CONTRIBUTIONS

AS conceived the project. BM collected and analysed data in Fig. 2, 3A-F, 4, 5a-d, cloned shRNA and MAP4 constructs and performed protein purification. DR performed Western blotting, cloning, glycerol gradients and all TIRF-based experiments in Fig. 5e-f, 6 and 7. ZR, DR and AS collected and analysed data for MT directionality and motility in Fig. 1,3 and 8. AS and BM wrote the manuscript.

ACKNOWLEDGEMENTS

We thank Pat Wadsworth (UMass, Amherst) for paGFP-Tubulin, Loren Looger (Janelia Farm) for mEos2-Tubulin, Stephen Royle (University of Warwick) for pRSET-PRC1, Andrew McAinsh (University of Warwick) for purified *Drosophila* kinesin, Ben Fitton for purified EB1-GFP, Ian Titley (ICR, London) and Muriel Erent (University of Warwick) for help with cell sorting. We are grateful to Rob Cross and Masanori Mishima for critical comments on the manuscript. This work was supported by funding from Marie Curie Cancer Care, the University of Warwick and the Lister Institute of Preventive Medicine to AS. AS is a Lister Institute Research Prize Fellow.

None of the authors of this manuscript have a financial interest related to this work.

REFERENCES

ADAMES, N. R. & COOPER, J. A. 2000. Microtubule interactions with the cell cortex causing nuclear movements in Saccharomyces cerevisiae. *J Cell Biol,* 149**,** 863-74.

AIZAWA, H., EMORI, Y., MORI, A., MUROFUSHI, H., SAKAI, H. & SUZUKI, K. 1991. Functional analyses of the domain structure of microtubule-associated protein-4 (MAP-U). *J Biol Chem,* 266**,** 9841-6.

ANTIN, P. B., FORRY-SCHAUDIES, S., FRIEDMAN, T. M., TAPSCOTT, S. J. & HOLTZER, H. 1981. Taxol induces postmitotic myoblasts to assemble interdigitating microtubule-myosin arrays that exclude actin filaments. *J Cell Biol,* 90**,** 300-8.

BICEK, A. D., TUZEL, E., DEMTCHOUK, A., UPPALAPATI, M., HANCOCK, W. O., KROLL, D. M. & ODDE, D. J. 2009. Anterograde microtubule transport drives microtubule bending in LLC-PK1 epithelial cells. *Mol Biol Cell,* 20**,** 2943-53.

BIELING, P., TELLEY, I. A. & SURREY, T. 2010. A minimal midzone protein module controls formation and length of antiparallel microtubule overlaps. *Cell,* 142**,** 420-32.

BISCHOFF, R. & HOLTZER, H. 1968. The effect of mitotic inhibitors on myogenesis in vitro. *J Cell Biol,* 36**,** 111-27.

BRANGWYNNE, C. P., MACKINTOSH, F. C., KUMAR, S., GEISSE, N. A., TALBOT, J., MAHADEVAN, L., PARKER, K. K., INGBER, D. E. & WEITZ, D. A. 2006. Microtubules can bear enhanced compressive loads in living cells because of lateral reinforcement. *J Cell Biol,* 173**,** 733-41.

BRAUN, M., DRUMMOND, D. R., CROSS, R. A. & MCAINSH, A. D. 2009. The kinesin-14 Klp2 organizes microtubules into parallel bundles by an ATP-dependent sorting mechanism. *Nat Cell Biol,* 11**,** 724-30.

BRAUN, M., LANSKY, Z., FINK, G., RUHNOW, F., DIEZ, S. & JANSON, M. E. 2011. Adaptive braking by Ase1 prevents overlapping microtubules from sliding completely apart. *Nat Cell Biol,* 13**,** 1259-64.

CHANG, W., WEBSTER, D. R., SALAM, A. A., GRUBER, D., PRASAD, A., EISERICH, J. P. & BULINSKI, J. C. 2002. Alteration of the C-terminal amino acid of tubulin specifically inhibits myogenic differentiation. *J Biol Chem,* 277**,** 30690-8.

CHEN, J., KANAI, Y., COWAN, N. J. & HIROKAWA, N. 1992. Projection domains of MAP2 and tau determine spacings between microtubules in dendrites and axons. *Nature,* 360**,** 674-7.

DAMMERMANN, A. & MERDES, A. 2002. Assembly of centrosomal proteins and microtubule organization depends on PCM-1. *J Cell Biol,* 159**,** 255-66.

DEVRED, F., BARBIER, P., DOUILLARD, S., MONASTERIO, O., ANDREU, J. M. & PEYROT, V. 2004. Tau induces ring and microtubule formation from alphabeta-tubulin dimers under nonassembly conditions. *Biochemistry,* 43**,** 10520-31.

ERICKSON, H. P. 2009. Size and shape of protein molecules at the nanometer level determined by sedimentation, gel filtration, and electron microscopy. *Biol Proced Online,* 11**,** 32-51.

FINK, G. 2006. Dynein-dependent Motility of Microtubules and Nucleation Sites Supports Polarization of the Tubulin Array in the Fungus Ustilago maydis. *Molecular Biology of the Cell,* 17**,** 3242-3253.

FINK, G., HAJDO, L., SKOWRONEK, K. J., REUTHER, C., KASPRZAK, A. A. & DIEZ, S. 2009. The mitotic kinesin-14 Ncd drives directional microtubule-microtubule sliding. *Nat Cell Biol,* 11**,** 717-23.

FOLKER, E. S., SCHULMAN, V. K. & BAYLIES, M. K. 2012. Muscle length and myonuclear position are independently regulated by distinct Dynein pathways. *Development,* 139**,** 3827-37.

GAILLARD, J., NEUMANN, E., VAN DAMME, D., STOPPIN-MELLET, V., EBEL, C., BARBIER, E., GEELEN, D. & VANTARD, M. 2008. Two microtubule-associated proteins of Arabidopsis MAP65s promote antiparallel microtubule bundling. *Mol Biol Cell,* 19**,** 4534-44.

GARNIER, J., GIBRAT, J. F. & ROBSON, B. 1996. GOR method for predicting protein secondary structure from amino acid sequence. *Methods Enzymol,* 266**,** 540-53.

GELL, C., FRIEL, C. T., BORGONOVO, B., DRECHSEL, D. N., HYMAN, A. A. & HOWARD, J. 2011. Purification of tubulin from porcine brain. *Methods Mol Biol,* 777**,** 15-28.

GRIMALDI, A. D., MAKI, T., FITTON, B. P., ROTH, D., YAMPOLSKY, D., DAVIDSON, M. W., SVITKINA, T., STRAUBE, A., HAYASHI, I. & KAVERINA, I. 2014. CLASPs are required for proper microtubule localization of end-binding proteins. *Dev Cell,* 30**,** 343-52.

GUNDERSEN, G. G., KHAWAJA, S. & BULINSKI, J. C. 1989. Generation of a stable, posttranslationally modified microtubule array is an early event in myogenic differentiation. *J Cell Biol,* 109**,** 2275-88.

HASAN, M. R., JIN, M., MATSUSHIMA, K., MIYAMOTO, S., KOTANI, S. & NAKAGAWA, H. 2006. Differences in the regulation of microtubule stability by the pro-rich region variants of microtubule-associated protein 4. *FEBS Lett,* 580**,** 3505-10.

HEALD, R., TOURNEBIZE, R., BLANK, T., SANDALTZOPOULOS, R., BECKER, P., HYMAN, A. & KARSENTI, E. 1996. Self-organization of microtubules into bipolar spindles around artificial chromosomes in Xenopus egg extracts. *Nature,* 382**,** 420-5.

HERNANDEZ, M. A., AVILA, J. & ANDREU, J. M. 1986. Physicochemical characterization of the heat-stable microtubule-associated protein MAP2. *Eur J Biochem,* 154**,** 41-8.

HOLTZER, H., CROOP, J., DIENSTMAN, S., ISHIKAWA, H. & SOMLYO, A. P. 1975. Effects of cytochaslasin B and colcemide on myogenic cultures. *Proc Natl Acad Sci U S A,* 72**,** 513-7.

JANKOVICS, F. & BRUNNER, D. 2006. Transiently Reorganized Microtubules Are Essential for Zippering during Dorsal Closure in Drosophila melanogaster. *Dev Cell,* 11**,** 375-385.

JANSON, M. E., LOUGHLIN, R., LOIODICE, I., FU, C., BRUNNER, D., NEDELEC, F. J. & TRAN, P. T. 2007. Crosslinkers and motors organize dynamic microtubules to form stable bipolar arrays in fission yeast. *Cell,* 128**,** 357-68.

JOLLY, A. L., KIM, H., SRINIVASAN, D., LAKONISHOK, M., LARSON, A. G. & GELFAND, V. I. 2010. Kinesin-1 heavy chain mediates microtubule sliding to drive changes in cell shape. *Proc Natl Acad Sci U S A,* 107**,** 12151-6.

KAPITEIN, L. C., PETERMAN, E. J., KWOK, B. H., KIM, J. H., KAPOOR, T. M. & SCHMIDT, C. F. 2005. The bipolar mitotic kinesin Eg5 moves on both microtubules that it crosslinks. *Nature,* 435**,** 114-8.

KAVERINA, I. & STRAUBE, A. 2011. Regulation of cell migration by dynamic microtubules. *Semin Cell Dev Biol,* 22**,** 968-74.

LOIODICE, I., STAUB, J., SETTY, T. G., NGUYEN, N. P., PAOLETTI, A. & TRAN, P. T. 2005. Ase1p organizes antiparallel microtubule arrays during interphase and mitosis in fission yeast. *Mol Biol Cell,* 16**,** 1756-68.

LU, W., FOX, P., LAKONISHOK, M., DAVIDSON, M. W. & GELFAND, V. I. 2013. Initial neurite outgrowth in Drosophila neurons is driven by kinesin-powered microtubule sliding. *Curr Biol,* 23**,** 1018-23.

MANGAN, M. E. & OLMSTED, J. B. 1996. A muscle-specific variant of microtubule-associated protein 4 (MAP4) is required in myogenesis. *Development,* 122**,** 771-81.

MATTIE, F. J., STACKPOLE, M. M., STONE, M. C., CLIPPARD, J. R., RUDNICK, D. A., QIU, Y., TAO, J., ALLENDER, D. L., PARMAR, M. & ROLLS, M. M. 2010. Directed microtubule growth, +TIPs, and kinesin-2 are required for uniform microtubule polarity in dendrites. *Curr Biol,* 20**,** 2169-77.

MCKINNEY, S. A., MURPHY, C. S., HAZELWOOD, K. L., DAVIDSON, M. W. & LOOGER, L. L. 2009. A bright and photostable photoconvertible fluorescent protein. *Nat Methods,* 6**,** 131-3.

MERDES, A., HEALD, R., SAMEJIMA, K., EARNSHAW, W. C. & CLEVELAND, D. W. 2000. Formation of spindle poles by dynein/dynactin-dependent transport of NuMA. *J Cell Biol,* 149**,** 851-62.

NGUYEN, H. L., CHARI, S., GRUBER, D., LUE, C. M., CHAPIN, S. J. & BULINSKI, J. C. 1997. Overexpression of full- or partial-length MAP4 stabilizes microtubules and alters cell growth. *J Cell Sci,* 110 (Pt 2)**,** 281-94.

NGUYEN, H. L., GRUBER, D., MCGRAW, T., SHEETZ, M. P. & BULINSKI, J. C. 1998. Stabilization and functional modulation of microtubules by microtubule-associated protein 4. *Biol Bull,* 194**,** 354-7.

NISHIYAMA, M., HIGUCHI, H. & YANAGIDA, T. 2002. Chemomechanical coupling of the forward and backward steps of single kinesin molecules. *Nat Cell Biol,* 4**,** 790-7.

ODDOUX, S., ZAAL, K. J., TATE, V., KENEA, A., NANDKEOLYAR, S. A., REID, E., LIU, W. & RALSTON, E. 2013. Microtubules that form the stationary lattice of muscle fibers are dynamic and nucleated at Golgi elements. *J Cell Biol,* 203**,** 205-13.

OOKATA, K., HISANAGA, S., BULINSKI, J. C., MUROFUSHI, H., AIZAWA, H., ITOH, T. J., HOTANI, H., OKUMURA, E., TACHIBANA, K. & KISHIMOTO, T. 1995. Cyclin B interaction with microtubule-associated protein 4 (MAP4) targets p34cdc2 kinase to microtubules and is a potential regulator of M-phase microtubule dynamics. *J Cell Biol,* 128**,** 849-62.

PIZON, V., GERBAL, F., DIAZ, C. C. & KARSENTI, E. 2005. Microtubule-dependent transport and organization of sarcomeric myosin during skeletal muscle differentiation. *EMBO J,* 24**,** 3781-92.

POHL, A. A., SUGNET, C. W., CLARK, T. A., SMITH, K., FUJITA, P. A. & CLINE, M. S. 2009. Affy exon tissues: exon levels in normal tissues in human, mouse and rat. *Bioinformatics,* 25**,** 2442-3.

RUSAN, N. M. 2004. Centrosome fragments and microtubules are transported asymmetrically away from division plane in anaphase. *J Cell Biol,* 168**,** 21-28.

RUSAN, N. M., TULU, U. S., FAGERSTROM, C. & WADSWORTH, P. 2002. Reorganization of the microtubule array in prophase/prometaphase requires cytoplasmic dynein-dependent microtubule transport. *J Cell Biol,* 158**,** 997-1003.

SAITOH, O., ARAI, T. & OBINATA, T. 1988. Distribution of microtubules and other cytoskeletal filaments during myotube elongation as revealed by fluorescence microscopy. *Cell Tissue Res,* 252**,** 263-73.

SAMORA, C. P., MOGESSIE, B., CONWAY, L., ROSS, J. L., STRAUBE, A. & MCAINSH, A. D. 2011. MAP4 and CLASP1 operate as a safety mechanism to maintain a stable spindle position in mitosis. *Nat Cell Biol,* 13**,** 1040-50.

SPENCER, J. A., ELIAZER, S., ILARIA, R. L., JR., RICHARDSON, J. A. & OLSON, E. N. 2000. Regulation of microtubule dynamics and myogenic differentiation by MURF, a striated muscle RING-finger protein. *J Cell Biol,* 150**,** 771-84.

SRSEN, V., FANT, X., HEALD, R., RABOUILLE, C. & MERDES, A. 2009. Centrosome proteins form an insoluble perinuclear matrix during muscle cell differentiation. *BMC Cell Biol,* 10**,** 28.

STRAUBE, A., HAUSE, G., FINK, G. & STEINBERG, G. 2006. Conventional kinesin mediates microtubule-microtubule interactions in vivo. *Mol Biol Cell,* 17**,** 907-16.

STRAUBE, A. & MERDES, A. 2007. EB3 regulates microtubule dynamics at the cell cortex and is required for myoblast elongation and fusion. *Curr Biol,* 17**,** 1318-25.

766 SUBRAMANIAN, R., WILSON-KUBALEK, E. M., ARTHUR, C. P., BICK, M. J., CAMPBELL, E. A.,
767 DARST, S. A., MILLIGAN, R. A. & KAPOOR, T. M. 2010. Insights into antiparallel microtubule
768 crosslinking by PRC1, a conserved nonmotor microtubule binding protein. *Cell,* 142**,** 433-43.
769 TANENBAUM, M. E., VALE, R. D. & MCKENNEY, R. J. 2013. Cytoplasmic dynein crosslinks and
770 slides anti-parallel microtubules using its two motor domains. *Elife,* 2**,** e00943.
771 TASSIN, A. M., MARO, B. & BORNENS, M. 1985. Fate of microtubule-organizing centers during
772 myogenesis in vitro. *J Cell Biol,* 100**,** 35-46.
773 TOBA, S., WATANABE, T. M., YAMAGUCHI-OKIMOTO, L., TOYOSHIMA, Y. Y. & HIGUCHI, H.
774 2006. Overlapping hand-over-hand mechanism of single molecular motility of cytoplasmic
775 dynein. *Proc Natl Acad Sci U S A,* 103**,** 5741-5.
776 TOYAMA, Y., FORRY-SCHAUDIES, S., HOFFMAN, B. & HOLTZER, H. 1982. Effects of taxol and
777 Colcemid on myofibrillogenesis. *Proc Natl Acad Sci U S A,* 79**,** 6556-60.
778 TRAPNELL, C., WILLIAMS, B. A., PERTEA, G., MORTAZAVI, A., KWAN, G., VAN BAREN, M. J.,
779 SALZBERG, S. L., WOLD, B. J. & PACHTER, L. 2010. Transcript assembly and
780 quantification by RNA-Seq reveals unannotated transcripts and isoform switching during cell
781 differentiation. *Nat Biotechnol,* 28**,** 511-5.
782 WAKELAM, M. J. 1985. The fusion of myoblasts. *Biochem J,* 228**,** 1-12.
783 WARREN, R. H. 1974. Microtubular organization in elongating myogenic cells. *J Cell Biol,* 63**,** 550-66.
784 WATERMAN-STORER, C. M., WORTHYLAKE, R. A., LIU, B. P., BURRIDGE, K. & SALMON, E. D.
785 1999. Microtubule growth activates Rac1 to promote lamellipodial protrusion in fibroblasts.
786 *Nat Cell Biol,* 1**,** 45-50.
787 WEST, R. R., TENBARGE, K. M. & OLMSTED, J. B. 1991. A model for microtubule-associated
788 protein 4 structure. Domains defined by comparisons of human, mouse, and bovine
789 sequences. *J Biol Chem,* 266**,** 21886-96.
790 WILSON, M. H. & HOLZBAUR, E. L. 2012. Opposing microtubule motors drive robust nuclear
791 dynamics in developing muscle cells. *J Cell Sci,* 125**,** 4158-69.
792 ZHANG, T., ZAAL, K. J., SHERIDAN, J., MEHTA, A., GUNDERSEN, G. G. & RALSTON, E. 2009.
793 Microtubule plus-end binding protein EB1 is necessary for muscle cell differentiation,
794 elongation and fusion. *J Cell Sci,* 122**,** 1401-9.

795

796

FIGURE LEGENDS

Figure 1: Microtubules are arranged in stable paraxial arrays during muscle cell differentiation. **(a)** Structured illumination microscopy of anti-tubulin stained C2C12 cells pre/post induction of muscle differentiation as indicated. Microtubule filaments have been manually traced to highlight arrangement. Scale bar 10µm. **(b)** Tracks of EB3-GFP in C2C12 cells at different stages of differentiation. Directionality is colour-coded (green and red: ±45º to longitudinal cell axis, blue and yellow: perpendicular to cell axis ±45º). Cell outlines are indicated with dashed white line. Scale bars 20µm. **(c)** Cummulative distribution of MT growth angles for example cells shown in (b). Kuiper statistics (K-S) is calculated as a measure for microtubule alignment as the sum of the maximum deviations d1 and d2 from a random distribution. See supplement 1 for angular histograms. **(d)** Average MT asymmetry of differentiating myoblasts. Data show mean ± SEM for 4-9 cells with >5000 microtubule tracks per condition. **(e-f)** Motility of paGFP-Tubulin labelled microtubule segments in myoblasts pre/post induction of differentiation and after depletion of dynein (shDHC) and kinesin-1 (shKHC). Bar-shaped patterns were activated perpendicular to the microtubule orientation using mCherry-Tubulin as marker (f). An individual bar-shaped activation pattern is shown in (e) for each condition. Arrows highlight microtubule-sliding events. Scale bars are 5µm. See supplementary Videos 1-5. **(g-h)** Frequency and velocity of microtubule sliding events observed following photoactivation of tubulin segments. Data show mean ± SEM, n = 17-51 activated patterns. Asterisks indicate significant difference from undifferentiated control cells (* $p<0.05$, ** $p<0.005$, *** $p<0.0005$). **(i)** Immunoblotting of C2C12 cell extracts pre/post induction of differentiation for DHC and KHC. Tubulin serves as loading control.

Figure 1–figure supplement 1: Microtubule growth orientation. Angular distribution of microtubule growth data obtained from EB3-GFP tracks for the cells shown in Figure 1b.

Figure 1–figure supplement 2: Dissipation of photoconverted microtubule labelling. Dissipation of photoconverted regions of mEos2-Tubulin in C2C12 cells before (undiff) and 48 hours post

induction of differentiation. Cells were treated with Taxol to stop dissipation by depolymerisation, or azide to stop dissipation by motor-driven movement. Data have been corrected for bleaching by substraction of data from cells treated with both Taxol and azide. Data show mean ± SEM, n=10-20 cells from 2 experiments. Half-life was determined from exponential decay curve fitted to the data.

Figure 1–figure supplement 3: Verification of dynein and kinesin depletion. Immunoblotting of C2C12 cell extracts from GFP-positive FACS-sorted cells treated with individual shRNAs for 72 hours probed with antibodies as indicated.

Figure 2: oMAP4 is required for myoblast elongation and fusion. (a) Domain organization of MAP4 isoforms. Green and red boxes represent isoform-specific regions in the projection domains of mMAP4 and oMAP4 respectively. Note that all three isoforms are expressed with 3, 4 or 5 tau-like MT binding repeats. **(b)** RT-PCR-based MAP4 expression analysis of RNA samples isolated from 0-60 hrs differentiated C2C12 cells. GAPDH was used as loading control. **(c-d)** Immunoblotting of extracts from 0-96 hrs differentiated C2C12 cells using antibodies against the N-terminus of oMAP4 (c) or the muscle-specific insertion of mMAP4 (d). Tubulin was used as a loading control. **(e)** Examples of shRNA-treated cells co-expressing GFP-Tubulin 48 hr after induction of differentiation. Scale bar 50µm. **(f, h)** Distribution of cell lengths after 48 hr differentiation following treatment with indicated shRNAs. 1,000-1,900 cells were measured from 3 independent experiments for each condition. Small triangles represent mean values. **(g, i)** Myoblast fusion analyses of C2C12 cells treated with indicated shRNAs after 56 hr differentiation.1,000-1,200 cells were analysed for each condition and only cells with three or more nuclei were scored as fused. Data are collected from 3 experiments for each condition and are presented as mean ± S.E.M. Asterisks indicate significant difference from shControl treatment or between pairs of samples as indicated (* $p<0.05$, ** $p<0.005$, *** $p<0.0005$).

Figure 2–figure supplement 1: Expression of major MAP4 isoforms. Relative transcript abundances of MAP4 isoforms during myoblast differentiation as determined by analysis of RNA sequencing data from undifferentiated and 60h differentiated C2C12 cells (Trapnell et al., 2010).

Comparative expression levels of MAP4 isoforms in several mouse tissues obtained by analysis of Affymetrix exon array data (Pohl et al., 2009). Data are shown as mean ± SD from 3 experiments for each tissue. See previously generated datasets 1-2 in supplement.

Figure 2–figure supplement 2: C2C12 cells express three major MAP4 isoforms with variable numbers of MT binding repeats. RT-PCR from total RNA isolated from C2C12 cells before (0hrs) and 48 hours post induction of differentiation with upstream primers specific for projection domains of uMAP4, mMAP4 and oMAP4 and downstream primer at 3' end of the MAP4 coding sequence to determine number of microtubule binding repeats. Digestion of PCR from 48 hour differentiated cells with exon-specific restriction nucleases to determine spliced exons that give rise to variants with different numbers of microtubule binding repeats.

Figure 2–figure supplement 3: Microtubular localization of eGFP-tagged MAP4 isoforms in C2C12 cells. Tubulin is used as a marker for microtubules. Scale bars are 20 μm, insets 2 μm.

Figure 2–figure supplement 4: Verification of mMAP4 depletion by immunofluorescence. Protein depletion was quantified by counting cells that expressed mMAP4 in GFP-Tubulin and shRNA co-expressing cells. Bars are 20 μm. 40-50 cells each were analysed for shControl and sh-mMAP4 transfections.

Figure 2–figure supplement 5: Verification of MAP4 depletion by immunoblotting. Immunoblotting of C2C12 cell extracts treated with individual shRNAs as indicated for 70-74 hours. Tubulin serves as loading control.

Figure 2–figure supplement 6: Verification of oMAP4 depletion and RNAi-protected rescue construct by immunoblotting. Immunoblot of whole cell extracts of HeLa cells co-transfected with shRNAs and control or rescue plasmids. Tubulin serves as loading control.

Figure 3: oMAP4 is required for the parallel arrangement of microtubules is differentiating muscle cells. (a-b) C2C12 myoblasts 48 hours after induction of differentiation treated with shRNA as indicated and stained for Myogenin (a marker for differentiating myoblasts, yellow), PCM-1 (red) and DAPI (blue). GFP-Tubulin (green) indicates successful transfection with shRNA. Insets show higher magnification of microtubule arrangement. Scale bars 25µm, 5µm in insets. **(c)** Timecourse of expression of embryonic myosin, a marker of myogenic differentiation. **(d)** Timecourse of relocalisation of PCM-1 from a focus around the centrosome to the surface of the nucleus. Cells with a complete nuclear ring were scored as positive. Data in c,d show mean ± SD, n = 30-50 cells from 2 experiments. **(e)** RNAi rescue experiment of delayed PCM-1 relocalisation phenotype. Data show mean ± SEM of 3 experiments with 50-60 cells each. **(f)** Timecourse of accumulation of cells with acetylated tubulin during muscle cell differentiation. Data in show mean ± SD, n = 30-50 cells from 2 experiments. **(g)** Manual tracing of microtubule filaments (yellow) relative to the longitudinal cell axis (red) in elongated mono-nucleated cells selected after 48h differentiation and shRNA treatment as indicated. Scale bars 10µm. See supplementary Videos 6-7. **(h)** Microtubule directionally from data as in g shown as cummulative frequency distribution. Data show mean ± SD, n = 3 experiments, 1522-1958 MTs. **(i)** Automatic tracking of EB3-tdTomato comets in elongated mono-nucleated cells selected after 48h differentiation and shRNA treatment as indicated. Direct lines from start to end of track are shown and colour-coded for direction relative to longitudinal axis of cell as indicated in legend. Scale bars 10µm. See supplementary Videos 8-9. **(j)** Distribution of microtubule growth angles obtained from data as in h. Data show mean ± SD, n = 3 experiments, 6251-6382 tracks. **(k-l)** Microtubule growth speed and duration was determined from EB tracks as in i. Pooled data shown as statistical box plots with percentiles as indicated.

Figure 3–figure supplement 1: Microtubule orientation in depleted cells. Manual segmentation of microtubules (white/black), their angular distribution relative to main cell axis (red), and cumulative

frequency of microtubule orientation following depletion of individual MAP4 isoforms and in oMAP4 RNAi rescue experiment. n≥10 cells. Kuiper statistic relative to random distribution is calculated as in Fig. 1c.

Figure 3–figure supplement 2: Microtubule growth orientation in depleted cells. Angular distribution of microtubule growth data from Figure 3j. To aid visualisation of data tails, bin size increases progressively between 0 and ±60º and is then constantly 30º.

Figure 4: oMAP4 prevents microtubule sliding in cells. (a) Microtubule motility (arrows) observed after photoconversion of mEOS2-Tubulin in 48 hours differentiated cells treated with shRNA as indicated. Scale bars 5µm. See supplementary Videos 10-11. **(b)** Frequency of microtubule motility events relative to average sliding velocity in 48 hours differentiated cells treated with shRNA as indicated. Data pooled from 3 experiments, n=15-23 cells. **(c-d)** Frequency of microtubule motility events: all events are shown in c, while only fast sliding events are shown in d. The latter were defined as movement faster than 700nm/s. Data show mean ± SD, n = 3 experiments, 15-23 cells. **(e)** Directionality of microtubule motility events. Paraxial movement is defined as occurring parallel to the long cell axis with a deviation less than 45º. Looping microtubules changed direction by more than 90º during the movement event. Data show mean ± SD, n = 3 experiments, 15-23 cells. **(f-g)** Expression of GFP-oMAP4 (upper row) or GFP-uMAP4 (lower row) in undifferentiated C2C12 cells stained with tubulin antibodies. The number of strong microtubule bundles (arrows) of at least 2µm length and three-fold intensity of an individual microtubule was scored. Data in g show mean ± SEM, n=13-23 cells. oMAP4 causes statistically significant change (p=0.02). Scale bar 20µm, 2µm in insets.

Figure 4–figure supplement 1: Microtubule orientation in depleted cells. Examples of microtubule traces (yellow) in dynein-depleted and dynein + oMAP4-depleted 48h differentiated elongated myoblasts, see Fig. 3g for examples for control and oMAP4 depletion. Angular distribution and cumulative frequency of microtubule orientation relative to the main cell axis (red) is shown for

933 data pooled from 3 experiments. Kuiper statistic relative to random distribution is calculated as in Fig.
934 1c.

935

936 **Figure 5: oMAP4 bundles microtubules *in vitro*. (a)** SDS-PAGE analysis of oMAP4 protein
937 purification. N-terminally 6xHis tagged full-length oMAP4 was puriified by Ni^{2+}-NTA affinity
938 chromatography followed by ion exchange chromatography. **(b)** Microtubule co-sedimentation
939 analysis of oMAP4 protein. Purified protein from (a) was incubated with Taxol-stabilised microtubules
940 prior to centrifugation. Separate centrifugations of microtubules alone and oMAP4 protein alone were
941 used as controls. Pellet and supernatant fractions were analysed by SDS-PAGE and Coomassie
942 staining. **(c-d)** Analysis of microtubule bundling by oMAP4 *in vitro*. Taxol- or GMP-CPP-stabilised
943 microtubules were incubated with buffer or 60nM purified oMAP4 protein before spreading on glass
944 for imaging. Insets show various microtubule crosslinking and bundling events. Scale bars 20μm, 5μm
945 in insets. **(e-f)** Comparison of bundling efficiency of oMAP4 with negative control (EB1) and positive
946 control (PRC1). Representative image and data quantified from >300 microtubules are shown. Scale
947 bar 10μm.

948

949 **Figure 6: oMAP4 zippers dynamic microtubules with a bias for antiparallel arrangements. (a)**
950 Dynamic Rhodamine-labelled microtubules (greyscale) assembled from immobilised Hilyte640-
951 labelled seeds (red) *in vitro* are zippered in the presence of oMAP4. Arrows highlight bundled
952 microtubules. Scale bar 10μm. **(b)** Histogram showing proportion of microtubule encounters leading to
953 MT zippering relative to microtubule encounter angles. Antiparallel encounters are observed at angles
954 above 90º. Note no zippering occurs between 25 and 150º. Data for GFP-oMAP4, EB1-GFP and
955 PRC1, each at 80nM concentration are shown for comparison. n = >400 microtubule encounters for
956 control and oMAP4, 136 encounters for PRC1 and 184 encounters for EB1. **(c)** Example of zippering
957 events (arrows) in the presence of 80nM oMAP4-GFP. Microtubule polarity is indicated with (+) at the
958 dynamic plus end. See supplementary Videos 12-13. Scale bar 10μm. **(d-e)** Immunoblot of oMAP4 in
959 fractions from glycerol gradients to determine its sedimentation coefficient with volume from top of
960 gradient indicated (d). Calibration curve using standard proteins with known sedimentation
961 coefficients and linear regression curve (e).

Figure 6–figure supplement 1: Microtubule length distribution in zippering experiments. For microtubule encounters between 10 and 30º incident angle in (near) parallel or (near) antiparallel orientation, the length of each microtubule was measured to the attached seed or the closest crossover point. None of the distributions are significantly different. n=22-54 encounters.

Figure 7: oMAP4 bundles can withstand motor forces. (a) Microtubule gliding assay on a *Drosophila* kinesin-1-coated surface. Time colour-coded projections over 30 seconds are shown for buffer control and 80nM oMAP4. **(b)** Instantaneous speeds of microtubule motility were determined from tracks of 50 microtubules and shown as histograms. The presence of 80nM oMAP4 reduces velocity of single microtubules by about 5%. **(c)** Microtubule bundles formed in solution by oMAP4 and landing on the kinesin-coated surface tend not to move (yellow filled arrows), while single microtubules do (green arrows). In about 25% of cases, bundles are driven apart by motor forces (magenta filled arrows) with microtubules gliding apart at normal speed once separated (magenta arrows). See supplementary Video 14. **(d)** Time colour-coded projection of gliding assay showing a microtubule bundle (arrow, appears white due to averaging of all time points) and individual microtubules over 447 seconds in the presence of 80nM oMAP4. **(e)** Instantaneous speeds of microtubule motility were determined from tracks of 20 single and bundled microtubules and shown as histograms. **(f)** Time between start of observation and either end of observation or time when bundle was separated by motor forces. Bundles that moved out of the field or dissociated as intact bundle were not scored.

Figure 8: oMAP4 and dynein co-operate in the organisation of the paraxial microtubule network in differentiating muscle cells. (a) Kuiper statistics of traced microtubule filaments as in Fig. 3g and Fig. 4 supplement 1 as a measure for microtubule orderliness is plotted against the mean cell length of 48 hrs differentiated C2C12 myoblasts treated with shRNAs as indicated. A linear fit to the data is shown. **(b)** We propose that the correlation between the precision of paraxial alignment and cell elongation suggests that ordered microtubule arrays confer higher mechanical stability to

counteract contractile forces. **(c)** Model of cooperation of oMAP4-mediated zippering with motor-driven microtubule sliding/transport in the formation of a highly ordered paraxial microtubule network. Microtubules are indicated in green, oMAP4 in magenta, dynein in blue and kinesin in purple.

VIDEO LEGENDS

Video 1: Photoconversion of mEos2-Tubulin in an undifferentiated C2C12 myoblast showing converted (left panel and magenta in right panel) and non-converted channels (middle panel and green in right panel). Scale bar: 10µm.

Video 2: Photoactivation of bar-shaped patterns of paGFP-Tubulin in an undifferentiated C2C12 myoblast. Scale bar: 10µm.

Video 3: Photoactivation of bar-shaped patterns of paGFP-Tubulin in a 94 hours differentiated C2C12 myoblast. Scale bar: 10µm.

Video 4: Photoactivation of bar-shaped patterns of paGFP-Tubulin in an undifferentiated C2C12 myoblast treated with shRNA against dynein heavy chain. Scale bar: 10µm.

Video 5: Photoactivation of bar-shaped patterns of paGFP-Tubulin in an undifferentiated C2C12 myoblast treated with shRNA against kinesin heavy chain (Kif5b). Scale bar: 10µm.

Video 6: Microtubule orientation in a 48 hours differentiated C2C12 myoblast treated with shControl co-expressing GFP-Tubulin. Manual tracing of microtubule cytoskeleton (yellow lines) and main cell axis (red line) shown as used for analysis. Scale bar: 10µm.

Video 7: Microtubule orientation in a 48 hours differentiated C2C12 myoblast treated with sh-oMAP4 co-expressing GFP-Tubulin. Manual tracing of microtubule cytoskeleton (yellow lines) and main cell axis (red line) shown as used for analysis. Scale bar: 10µm.

Video 8: Growing microtubules in a 48 hours differentiated C2C12 myoblast treated with sh-Control co-expressing EB3-tdTomato. Scale bar: 10µm.

Video 9: Growing microtubules in a 48 hours differentiated C2C12 myoblast treated with sh-oMAP4 co-expressing EB3-tdTomato. Scale bar: 10µm.

Video 10: Photoconversion of bar-shaped patterns of mEOS2-Tubulin in a 48 hours differentiated C2C12 myoblast treated with shControl. Scale bar: 10µm.

Video 11: Photoconversion of bar-shaped patterns of mEOS2-Tubulin in a 48 hours differentiated C2C12 myoblast treated with sh-oMAP4. Scale bar: 10µm.

Video 12: TIRF-based assay showing dynamic Rhodamine-labelled microtubules assembled from immobilised seeds. Scale bar: 10µm.

Video 13: TIRF-based assay showing dynamic microtubules in the presence of 80nM GFP-oMAP4. Note that antiparallel microtubule encounters result in zippering into an antiparallel bundle in most cases. Scale bar: 10µm.

Video 14: Microtubule gliding assay on a kinesin-1 coated surface in the presence of 80nM GFP-oMAP4. Note that single microtubules move persistently, while bundles don't until they are driven apart. Scale bar: 10µm.

SUPPLEMENTARY FILES

Supplementary file 1: RNAseq_Myoblast_Myocyte: RNA sequencing data for C2C12 myoblasts and 60h differentiated myocytes (Trapnell et al., 2010) extracted for four regions in MAP4 as shown in Fig. 2 supplement 1.

Supplementary file 2: Affymetrix Exon Arrays: Affymetrix exon array data (Pohl et al., 2009) for four regions in MAP4 as shown in Fig. 2 supplement 1.

SOURCE CODE FILES

source code 1 MATLAB code MTdirectionality: Custom MATLAB function to compute directionality of MT growth relative to the main cell axis, generate figure with tracks colour-coded for direction, plot angular histograms and calculate Kuiper statistics relative to a random distribution.

Figure 1

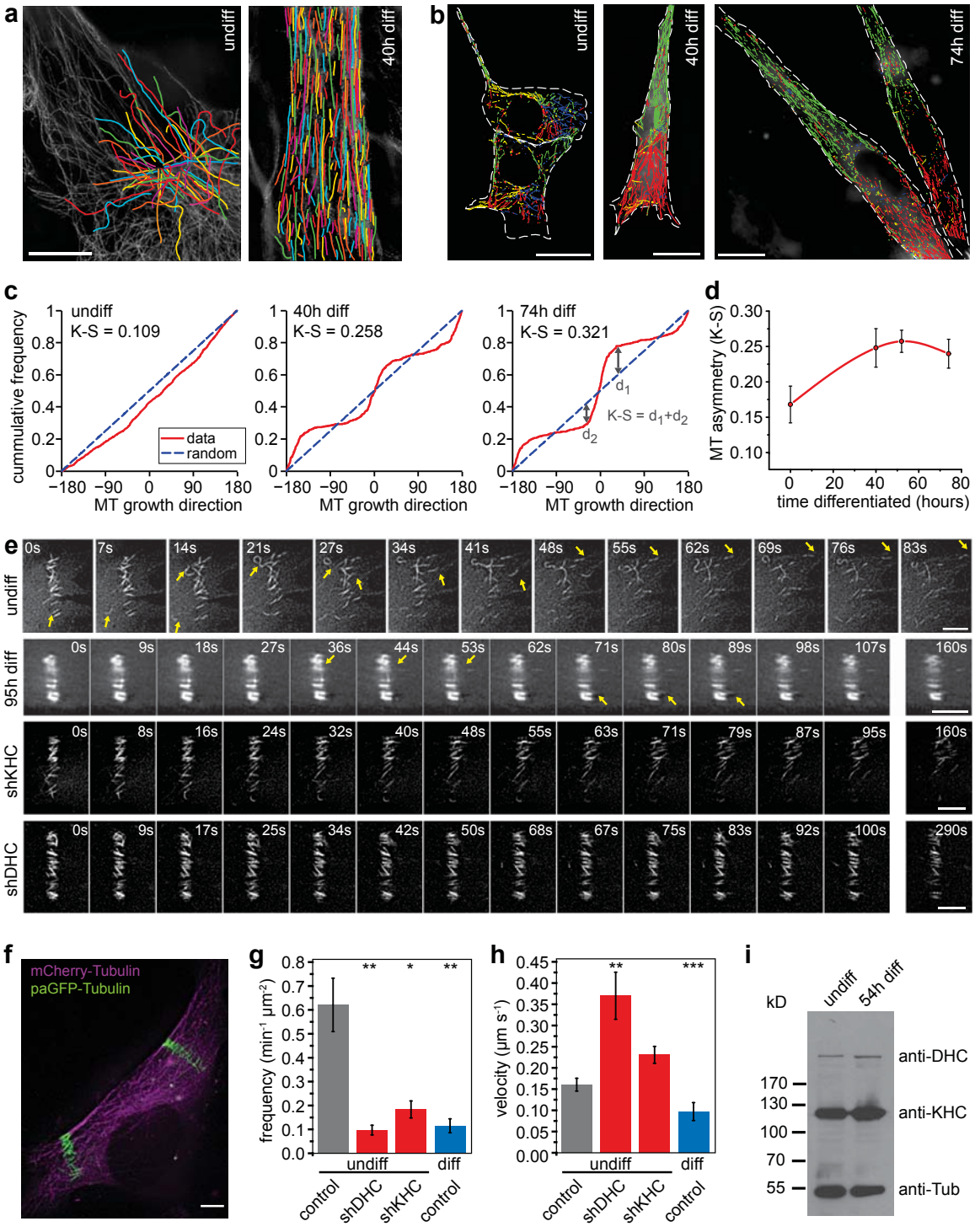
a
undiff
40h diff
b
undiff
40h diff
74h diff
c
undiff
K-S = 0.109
40h diff
K-S = 0.258
74h diff
K-S = 0.321
cummulative frequency
data
random
MT growth direction
d1
d2
K-S = d1+d2
d
MT asymmetry (K-S)
time differentiated (hours)
e
undiff
95h diff
shKHC
shDHC
f
mCherry-Tubulin
paGFP-Tubulin
g
frequency (min-1 µm-2)
undiff
diff
control
shDHC
shKHC
control
h
velocity (µm s-1)
undiff
diff
control
shDHC
shKHC
control
i
kD
undiff
54h diff
170
130
100
70
55
anti-DHC
anti-KHC
anti-Tub

Figure 2

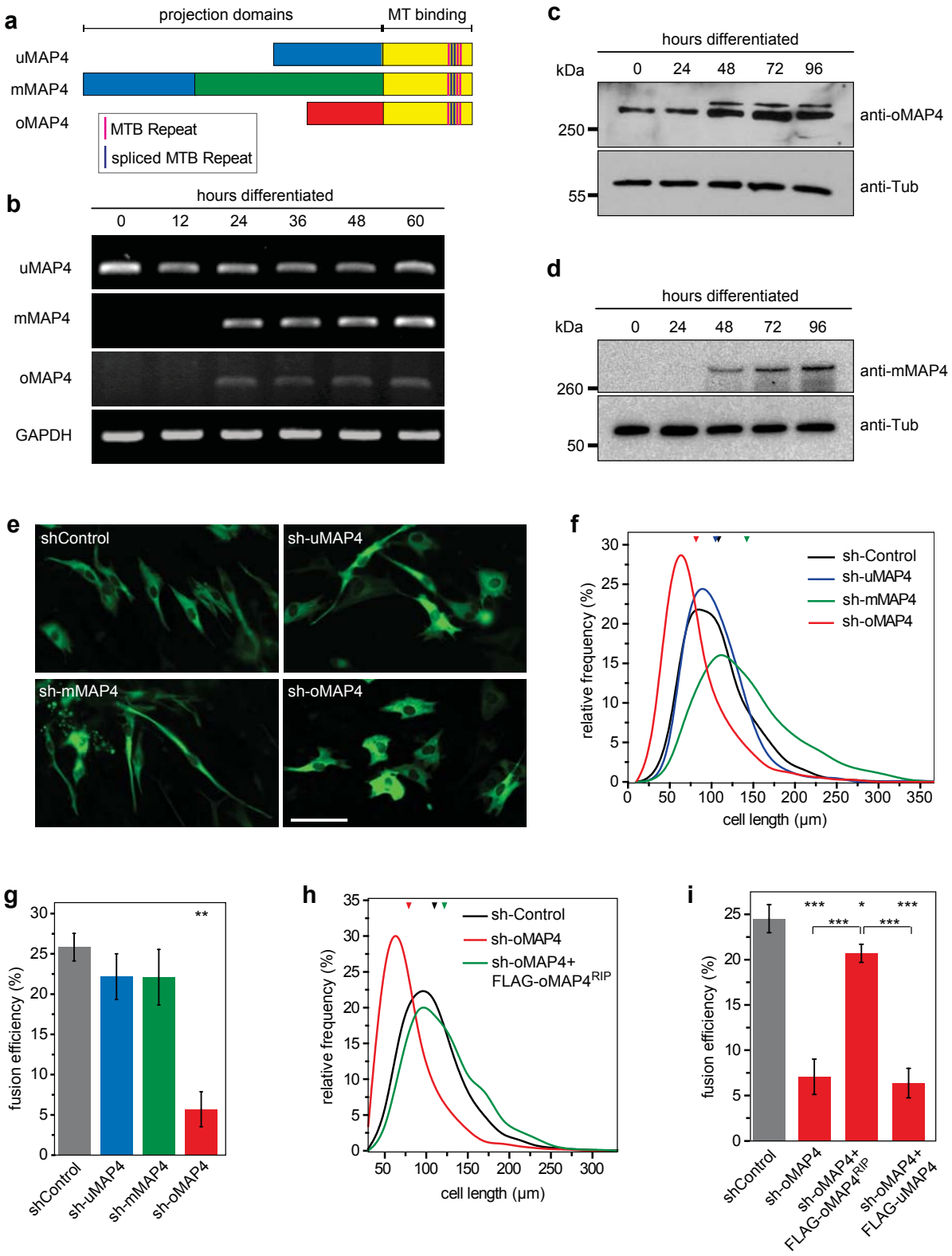
a
projection domains
MT binding
uMAP4
mMAP4
oMAP4
MTB Repeat
spliced MTB Repeat
b
hours differentiated
0 12 24 36 48 60
uMAP4
mMAP4
oMAP4
GAPDH
c
hours differentiated
kDa
0 24 48 72 96
250
55
anti-oMAP4
anti-Tub
d
hours differentiated
kDa
0 24 48 72 96
260
50
anti-mMAP4
anti-Tub
e
shControl
sh-uMAP4
sh-mMAP4
sh-oMAP4
f
sh-Control
sh-uMAP4
sh-mMAP4
sh-oMAP4
relative frequency (%)
cell length (μm)
g
fusion efficiency (%)
**
shControl
sh-uMAP4
sh-mMAP4
sh-oMAP4
h
sh-Control
sh-oMAP4
sh-oMAP4+
FLAG-oMAP4RIP
relative frequency (%)
cell length (μm)
i
fusion efficiency (%)
***
*
***
***
***
shControl
sh-oMAP4
sh-oMAP4+
FLAG-oMAP4RIP
sh-oMAP4+
FLAG-uMAP4

Figure 3

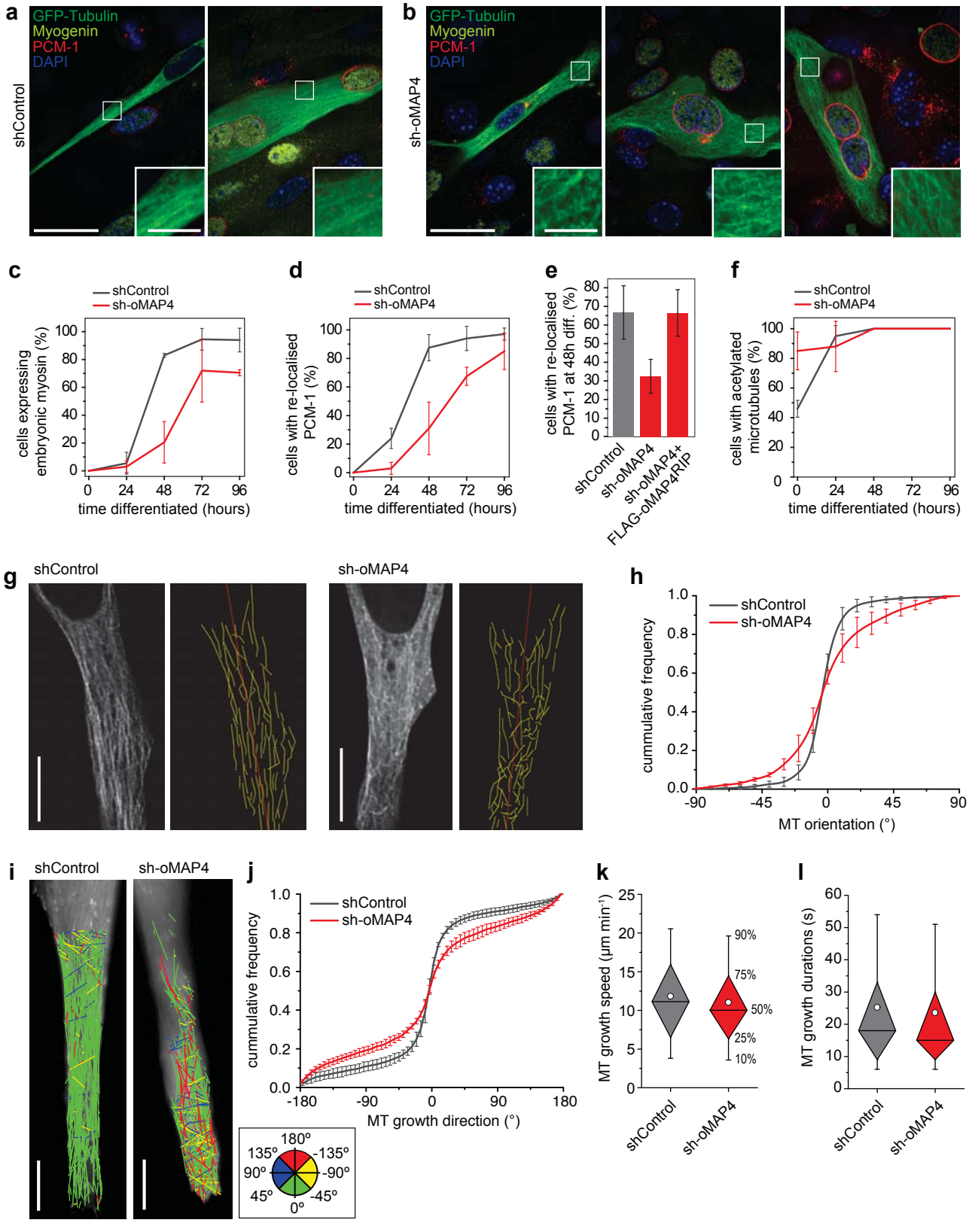
a
GFP-Tubulin
Myogenin
PCM-1
DAPI
shControl
b
GFP-Tubulin
Myogenin
PCM-1
DAPI
sh-oMAP4
c
shControl
sh-oMAP4
cells expressing embryonic myosin (%)
time differentiated (hours)
d
shControl
sh-oMAP4
cells with re-localised PCM-1 (%)
time differentiated (hours)
e
cells with re-localised PCM-1 at 48h diff. (%)
shControl
sh-oMAP4
sh-oMAP4+ FLAG-oMAP4RIP
f
shControl
sh-oMAP4
cells with acetylated microtubules (%)
time differentiated (hours)
g
shControl
sh-oMAP4
h
shControl
sh-oMAP4
cummulative frequency
MT orientation (°)
i
shControl
sh-oMAP4
j
shControl
sh-oMAP4
cummulative frequency
MT growth direction (°)
180°
135°
-135°
90°
-90°
45°
-45°
0°
k
MT growth speed (μm min-1)
90%
75%
50%
25%
10%
shControl
sh-oMAP4
l
MT growth durations (s)
shControl
sh-oMAP4

Figure 4

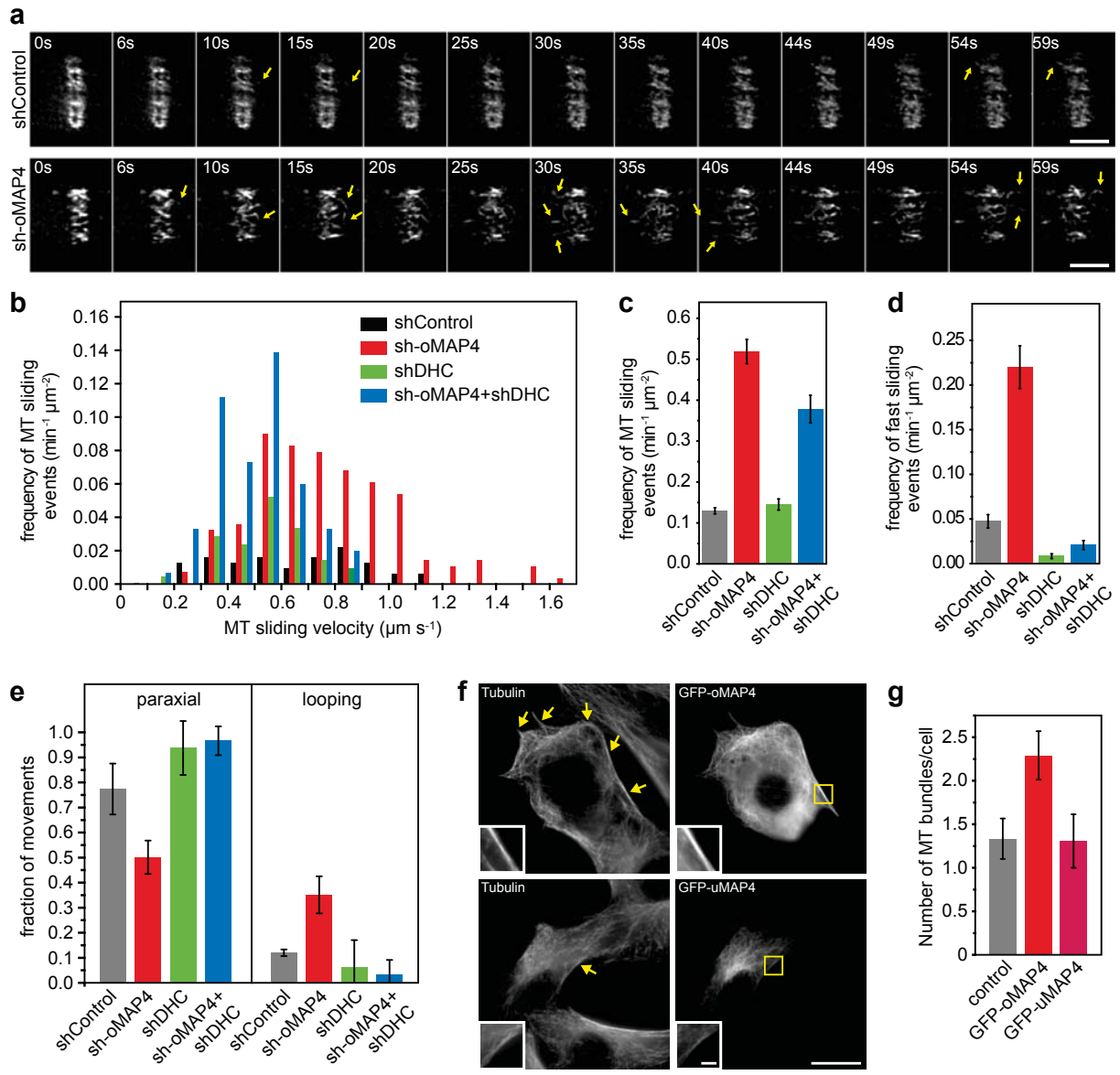
a
shControl
sh-oMAP4
0s
6s
10s
15s
20s
25s
30s
35s
40s
44s
49s
54s
59s
b
frequency of MT sliding events (min-1 µm-2)
MT sliding velocity (µm s-1)
shControl
sh-oMAP4
shDHC
sh-oMAP4+shDHC
c
frequency of MT sliding events (min-1 µm-2)
d
frequency of fast sliding events (min-1 µm-2)
e
paraxial
looping
fraction of movements
f
Tubulin
GFP-oMAP4
GFP-uMAP4
g
Number of MT bundles/cell
control
GFP-oMAP4
GFP-uMAP4

Figure 5

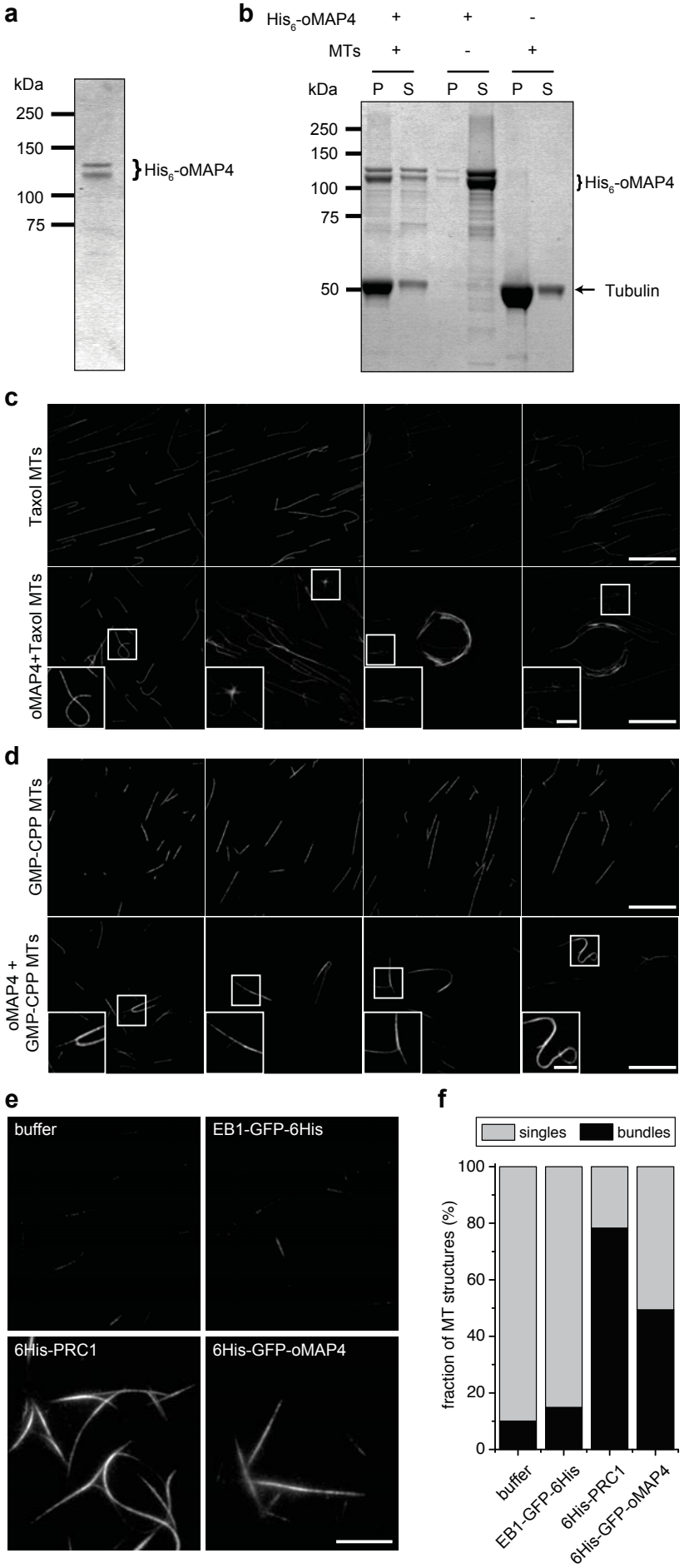
a
kDa
250
150
100
75
His6-oMAP4
b
His6-oMAP4 + + -
MTs + - +
kDa
P S P S P S
250
150
100
75
50
His6-oMAP4
Tubulin
c
Taxol MTs
oMAP4+Taxol MTs
d
GMP-CPP MTs
oMAP4 + GMP-CPP MTs
e
buffer
EB1-GFP-6His
6His-PRC1
6His-GFP-oMAP4
f
singles
bundles
fraction of MT structures (%)
0
20
40
60
80
100
buffer
EB1-GFP-6His
6His-PRC1
6His-GFP-oMAP4

Figure 6

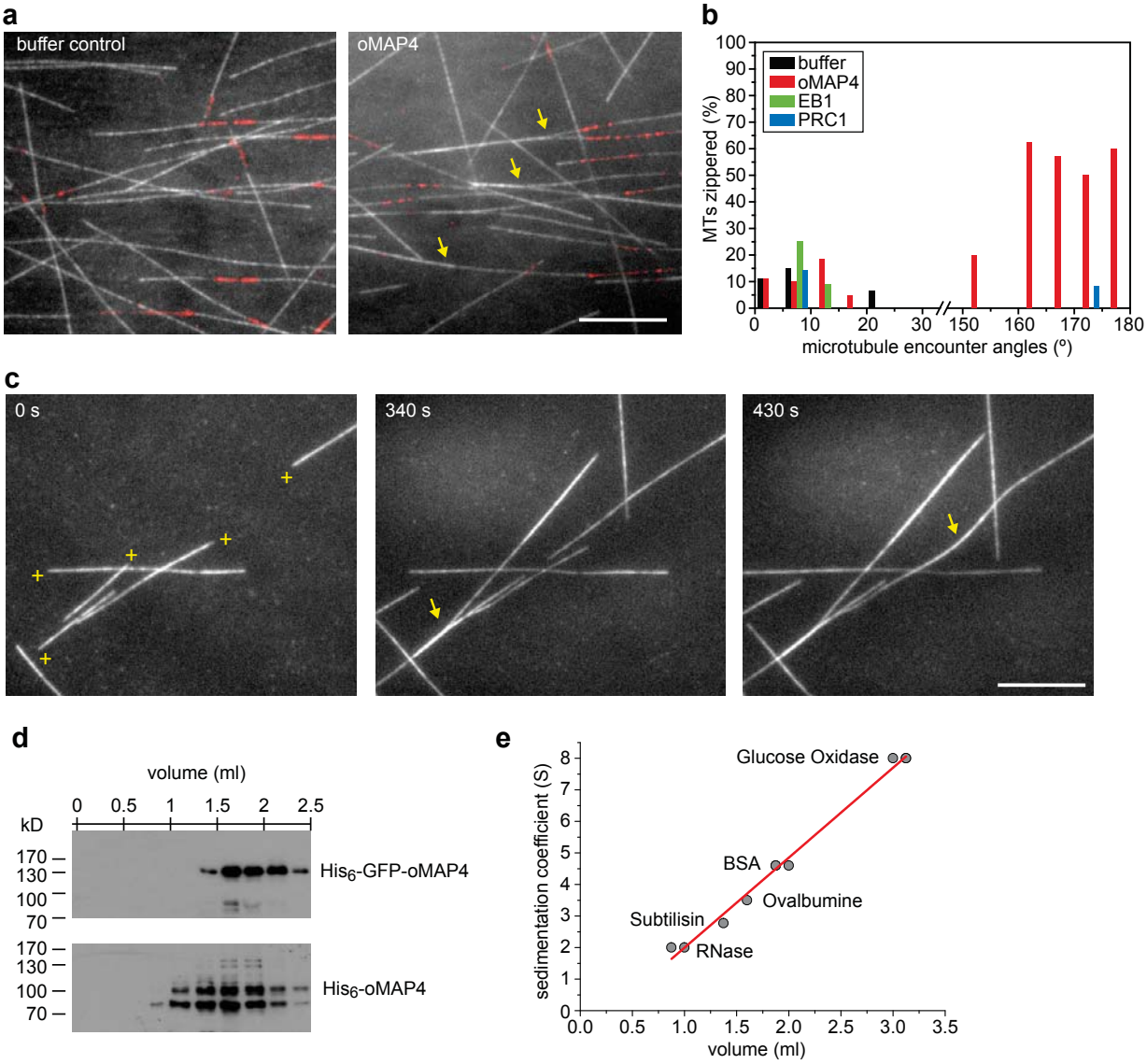
a
buffer control
oMAP4
b
buffer
oMAP4
EB1
PRC1
MTs zippered (%)
microtubule encounter angles (º)
c
0 s
340 s
430 s
d
volume (ml)
kD
His6-GFP-oMAP4
His6-oMAP4
e
Glucose Oxidase
BSA
Ovalbumine
Subtilisin
RNase
sedimentation coefficient (S)
volume (ml)

Figure 7

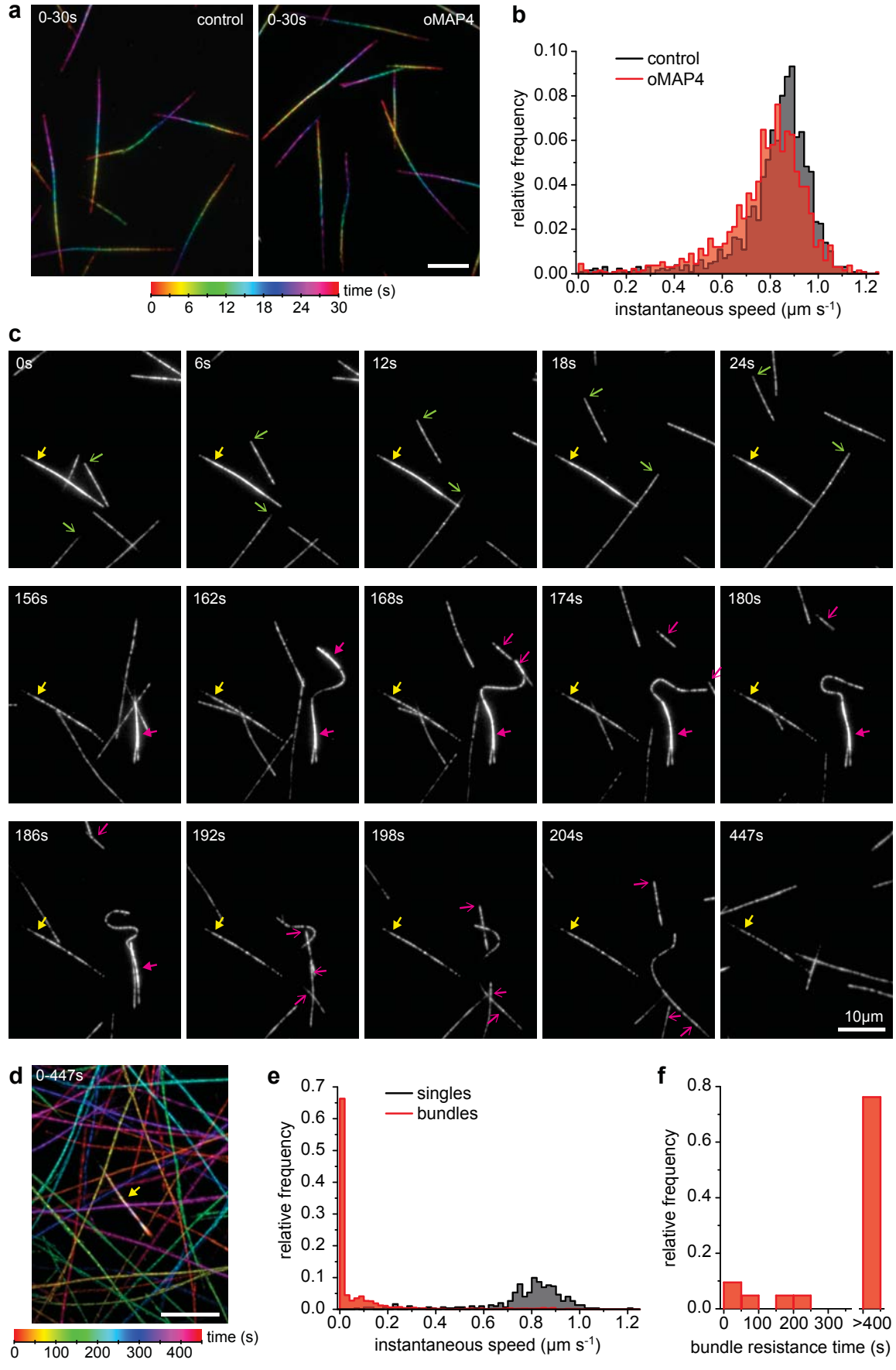
a
0-30s
control
0-30s
oMAP4
time (s)
0 6 12 18 24 30
b
control
oMAP4
relative frequency
0.00 0.02 0.04 0.06 0.08 0.10
0.0 0.2 0.4 0.6 0.8 1.0 1.2
instantaneous speed (μm s-1)
c
0s
6s
12s
18s
24s
156s
162s
168s
174s
180s
186s
192s
198s
204s
447s
10μm
d
0-447s
time (s)
0 100 200 300 400
e
singles
bundles
relative frequency
0.0 0.1 0.2 0.3 0.4 0.5 0.6 0.7
0.0 0.2 0.4 0.6 0.8 1.0 1.2
instantaneous speed (μm s-1)
f
relative frequency
0.0 0.2 0.4 0.6 0.8
0 100 200 300 >400
bundle resistance time (s)

Figure 8

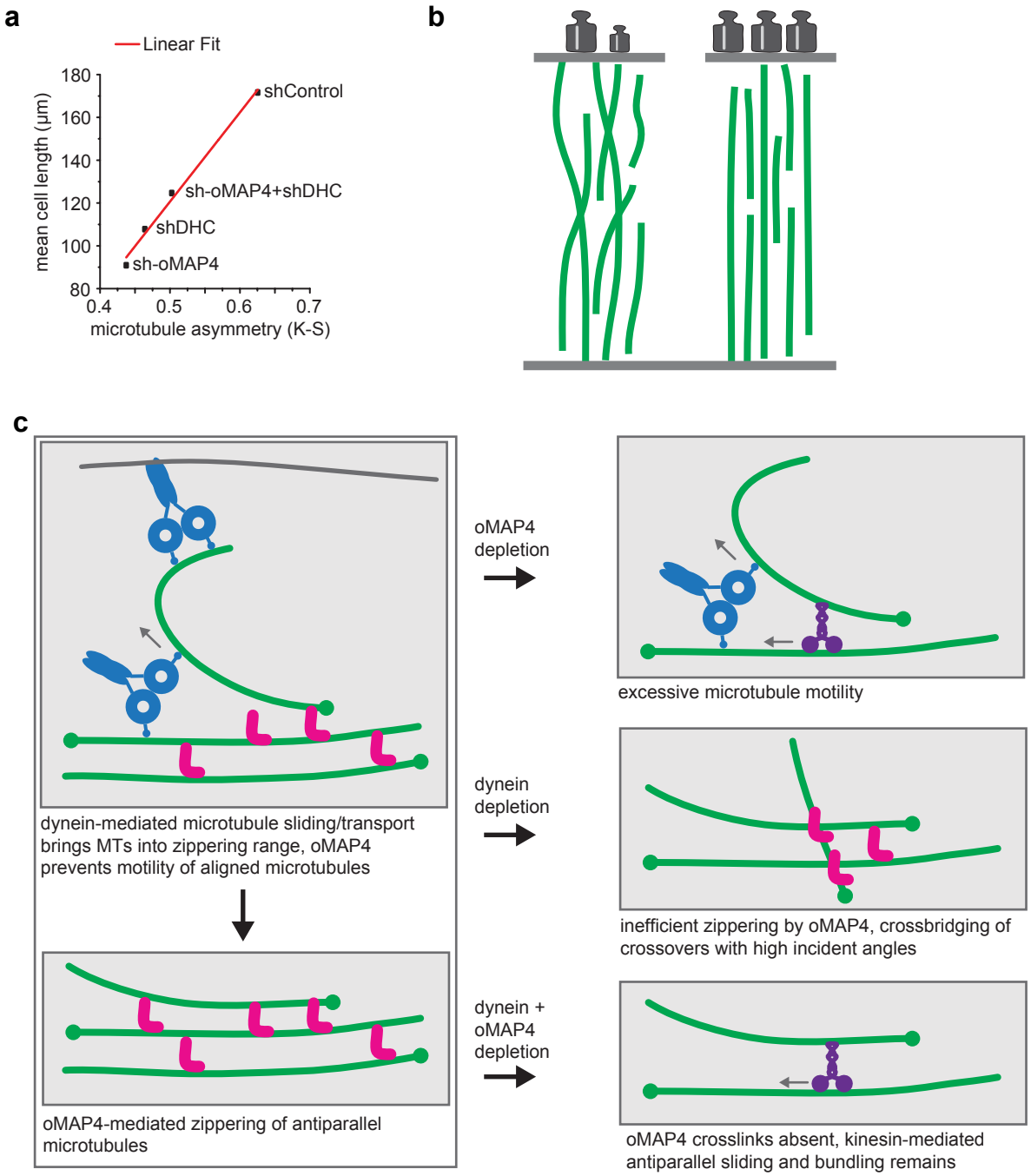
a
Linear Fit
mean cell length (µm)
180
160
140
120
100
80
0.4
0.5
0.6
0.7
microtubule asymmetry (K-S)
shControl
sh-oMAP4+shDHC
shDHC
sh-oMAP4
b
c
dynein-mediated microtubule sliding/transport brings MTs into zippering range, oMAP4 prevents motility of aligned microtubules
oMAP4-mediated zippering of antiparallel microtubules
oMAP4 depletion
excessive microtubule motility
dynein depletion
inefficient zippering by oMAP4, crossbridging of crossovers with high incident angles
dynein + oMAP4 depletion
oMAP4 crosslinks absent, kinesin-mediated antiparallel sliding and bundling remains